Centrality dependence of π, K, and p production in Pb-Pb collisions at √sNN = 2.76 TeV

(ALICE Collaboration) Abelev, B.; ...; Antičić, Tome; ...; Gotovac, Sven; ...; Mudnić, Eugen; ...; Planinić, Mirko; ...; ...

Journal article, Published version
Rad u časopisu, Objavljena verzija rada (izdavačev PDF)

Permanent link / Trajna poveznica: https://urn.nsk.hr/urn:nbn:hr:217:459494

Download date / Datum preuzimanja: **2025-04-01**

Repository / Repozitorij:

Repository of the Faculty of Science - University of Zagreb

Centrality dependence of π, K, and p production in Pb-Pb collisions at $\sqrt{s_{NN}} = 2.76$ TeV

B. Abelev *et al.*[*]

(ALICE Collaboration)

In this paper measurements are presented of $\pi^{\pm}$, $K^{\pm}$, p, and $\bar{p}$ production at midrapidity ($|y| < 0.5$), in Pb-Pb collisions at $\sqrt{s_{NN}} = 2.76$ TeV as a function of centrality. The measurement covers the transverse-momentum (p_T) range from 100, 200, and 300 MeV/c up to 3, 3, and 4.6 GeV/c for π, K, and p, respectively. The measured p_T distributions and yields are compared to expectations based on hydrodynamic, thermal and recombination models. The spectral shapes of central collisions show a stronger radial flow than measured at lower energies, which can be described in hydrodynamic models. In peripheral collisions, the p_T distributions are not well reproduced by hydrodynamic models. Ratios of integrated particle yields are found to be nearly independent of centrality. The yield of protons normalized to pions is a factor $\sim$1.5 lower than the expectation from thermal models.

I. INTRODUCTION

The ultimate goal of heavy-ion collisions is the study of the properties of a deconfined and chirally restored state of matter: the quark-gluon plasma (QGP). Indications of its existence have been already provided by previous studies at the CERN Super Proton Synchrotron (SPS) [1] and at the Relativistic Heavy Ion Collider (RHIC) [2–6]. With the advent of the Large Hadron Collider (LHC) a new energy regime is being studied, aiming at a precise characterization of the QGP properties.

The matter created in heavy-ion collisions exhibits strong collectivity, behaving as a nearly perfect liquid as observed at RHIC [7,8]. Its collective properties can be studied through transverse-momentum (p_T) distributions of identified particles. A solid understanding of the bulk properties of the expanding fireball is necessary for the interpretation of many observables. Any signal produced in the QGP phase has to be folded with the space-time evolution of the whole system, which has to be taken into account for comparison of theory and data.

Models based on relativistic hydrodynamics have been very successful in describing observables such as the transverse-momentum distributions of identified particles, up to a few GeV/c. These distributions contain information about the transverse expansion and the temperature at the moment when the hadrons decouple from the system [9,10]. It is commonly assumed that a significant fraction of the collective flow builds up in the expansion of the fireball in the initial partonic phase [8]. In this picture, the system would cool down as a consequence of the expansion and undergo a phase transition from a partonic to a hadronic phase. The hadrons continue to interact, building up additional collective flow and potentially changing the relative abundances. The hadronic yields are fixed at the moment when inelastic collisions no longer play a role

in the system [11–14]. However, it is usually assumed that the hadronic phase does not affect particle abundances [10,15]. It was also suggested that the temperature of the hadronic ("chemical") freeze-out can be related to the phase transition temperature [12,16,17]. Abundances of particles have been fitted very successfully over a wide range of energies (from $\sqrt{s_{NN}} = 2$ GeV to $\sqrt{s_{NN}} = 200$ GeV [11,12,14]) with thermal (or "statistical hadronization") models. From these fits, one can extract the thermal properties of the system at the moment when the particle abundances are fixed, the key parameters being the "chemical freeze-out" temperature T_{ch} and the baryochemical potential μ_B (determined by the net baryon content of the system). As will be discussed, the new data presented in this work seem to question part of the assumptions in these models, as also reported in Ref. [18]. The system eventually decouples when elastic interactions cease, at the "kinetic freeze-out" temperature T_{kin}. This temperature, together with the expansion velocity at the moment of decoupling, can be inferred from the p_T distributions of identified particles.

In the intermediate p_T region ($2 \lesssim p_T \lesssim 8$ GeV/c) the baryon-to-meson ratios have been shown to reach values $\gtrsim 1$ for $p_T \sim 3$ GeV/c, much larger than in pp collisions [19]. It was suggested that this could be a consequence of hadronization via recombination of quarks from the plasma (in the coalescence models [20,21]).

In this paper, we present the measurement of p_T spectra of $\pi^{\pm}$, $K^{\pm}$, p, and $\bar{p}$ in Pb-Pb collisions at $\sqrt{s_{NN}} = 2.76$ TeV as a function of centrality and over a wide p_T range (from 100, 200, 300 MeV/c up to 3, 3, 4.6 GeV/c, for π, K, and p, respectively). The ALICE experiment, thanks to its unique particle identification (PID) capabilities, is well suited for these measurements. Previous results on identified particle production in pp collisions have been reported in Ref. [22].

The paper is organized as follows. In Sec. II the data sample and the analysis technique are discussed. The systematic uncertainties are presented in Sec. III and the results in Sec. IV. These are discussed in the context of theoretical models in Sec. V. Finally, we come to our conclusions in Sec. VI.

II. DATA SAMPLE AND ANALYSIS METHOD

The data used for this analysis were collected during the first Pb-Pb run at the Large Hadron Collider in fall 2010.

---

[*]Full author list given at the end of the article.

The sample consists of about 4 million events, after event selection.

A detailed description of the ALICE detector can be found in Refs. [23,24]. The central tracking and PID detectors used in this work cover the pseudorapidity range $|\eta| < 0.9$ and are, from the innermost one outward, the Inner Tracking System (ITS), the Time Projection Chamber (TPC), the Transition Radiation Detector (TRD), and the Time-Of-Flight array (TOF). The detector features a small material budget (~ 0.1 X/X_0 for particles going through the TPC) and a low magnetic field, which allow for the reconstruction of low-p_T particles. The central detectors are embedded in a 0.5-T solenoidal field, whose polarity was reversed to allow for systematic studies.

A pair of forward scintillator hodoscopes, the VZERO detectors ($2.8 < \eta < 5.1$ and $-3.7 < \eta < -1.7$), measured the arrival time of particles with a resolution of 1 ns and was used for triggering purposes and centrality determination. The data were collected using a minimum bias trigger requiring a combination of hits in the two innermost layers of the ITS (Silicon Pixel Detector, SPD, see below) and in the VZERO. The trigger condition used during the data-taking has been changed as a function of time to cope with the increasing luminosity delivered by the LHC. This time dependence was eliminated off-line by requiring two hits in the SPD and one hit in either of the VZERO detectors. This condition was shown to be fully efficient for the 90% most central events [25].

The signal in the VZERO was required to lie in a narrow time window of about 30 ns around the nominal collision time, in order to reject any contamination from beam-induced backgrounds. Only events produced in the vertex fiducial region of $|V_z| < 10$ cm were considered in the analysis (where V_z is the vertex position along the beam direction). In the sample used for this analysis, a non-negligible fraction of the ions were located outside of their nominal radio-frequency bucket in the bunch, giving rise to "satellite" collisions. These events are produced well outside the vertex fiducial region but could give rise to "fake" vertices due to the combinatorial algorithm which reconstructs the vertices assuming that particles are coming from the area around the nominal region. These events were rejected, cutting on the correlation of arrival times of beam fragments to a pair of zero-degree calorimeters (ZDCs), placed close to the beam pipe, 114 m away from the interaction point on either side of the detector. For details, see Refs. [26,27].

The VZERO amplitude distribution was also used to determine the centrality of the events. In a first step, it was fitted with a Glauber Monte Carlo model to compute the fraction of the hadronic cross section corresponding to any given range of the VZERO amplitude. Based on these studies, the data were divided into several centrality percentiles, selecting on signal amplitudes measured in the VZERO [25]. The results in this paper are reported in 10 centrality bins, ranging from 0–5% to 80–90%, The centrality intervals and the corresponding charged-particle multiplicity measured in $|\eta| < 0.5$ (called $dN_{ch}/d\eta$ in the following) are summarized in Sec. IV. The $dN_{ch}/d\eta$ in the centrality bin 80–90%, shown here for the first time, was computed with the same analysis as described in Ref. [26]. The contamination from electromagnetic processes is negligible down to 80% centrality. In the bin 80–90% an upper limit for this contribution was estimated as 6%, using

TABLE I. p_T range (GeV/c) covered by the different analyses.

Analysis	π	K	p
ITS stand-alone	0.10–0.60	0.20–0.50	0.30–0.60
TPC/TOF	0.20–1.20	0.25–1.20	0.45–1.80
TOF fits	0.50–3.00	0.45–3.00	0.50–4.60

the energy distributions of the ZDCs and looking for the single (or few) neutron peaks on top of the distribution which would be expected for hadronic interactions [25,28].

The production of $\pi^{\pm}$, $K^{\pm}$, p, and $\bar{p}$ was measured at midrapidity ($|y| < 0.5$) via three independent analyses, each one focusing on a subrange of the total p_T distribution, with emphasis on the individual detectors and specific techniques to optimize the signal extraction. The ranges covered by the three analyses are summarized in Table I.

The ITS is composed of six layers of silicon detectors using three different technologies. The two innermost layers, based on a silicon pixel technology (SPD), are also used in the trigger logic, as they provide online the number of pixel chips hit by the produced particles, as mentioned above. The four outer layers, made of drift (SDD) and strip (SSD) detectors, provide identification via the specific energy loss. Moreover, using the ITS as a stand-alone tracker enables the reconstruction and identification of particles that do not reach the TPC (at low momentum) or cross its dead sectors. This makes the identification of π, K, and p possible down to, respectively, 0.1, 0.2, and 0.3 GeV/c in p_T. In the first analysis, "ITS stand-alone" tracks and dE/dx were used. At least four points are required to form a track, from which at least 1 must be in the SPD and three in the drift or strip detectors. With such a small number of tracking points and the high multiplicity in central heavy-ion collisions, the probability of having tracks with wrongly associated clusters is not negligible. This contribution is strongly suppressed by applying a cut on the χ^2 per cluster <2.5 and not allowing tracks to share clusters. These cuts, however, introduce a strong centrality dependence of the efficiency, as shown in Figs. 1(a), 1(b), and 1(c). The efficiency saturates at ~ 0.6 mostly due to the requirement of an SPD point: This detector was only $\sim 80\%$ operational in 2010 [29]. For each track, the dE/dx is calculated using a truncated mean: the average of the lowest two points in case four points are measured or a weighted sum of the lowest (weight 1) and the second-lowest point (weight 1/2) in case only three points are measured. The final dE/dx resolution is about 10%. The particle identity was assigned according to the distance, measured in units of the resolution, from the expected energy loss curves. While no upper limit on this distance was, in general, used, a 2σ lower bound was applied in the case of pions to remove contamination from electrons at low p_T. The procedure results in asymmetric ranges around the curves for π, K, and p to reflect the asymmetric nature of the energy loss (Fig. 2, top). The range of this analysis is determined at low p_T by the ITS stand-alone tracking efficiency and at high p_T by the contamination from other particle species: The analysis is stopped when the systematic uncertainty coming from this is no longer negligible.

The other two analyses were based on global tracks, which combine the information from the ITS, the TPC, and the
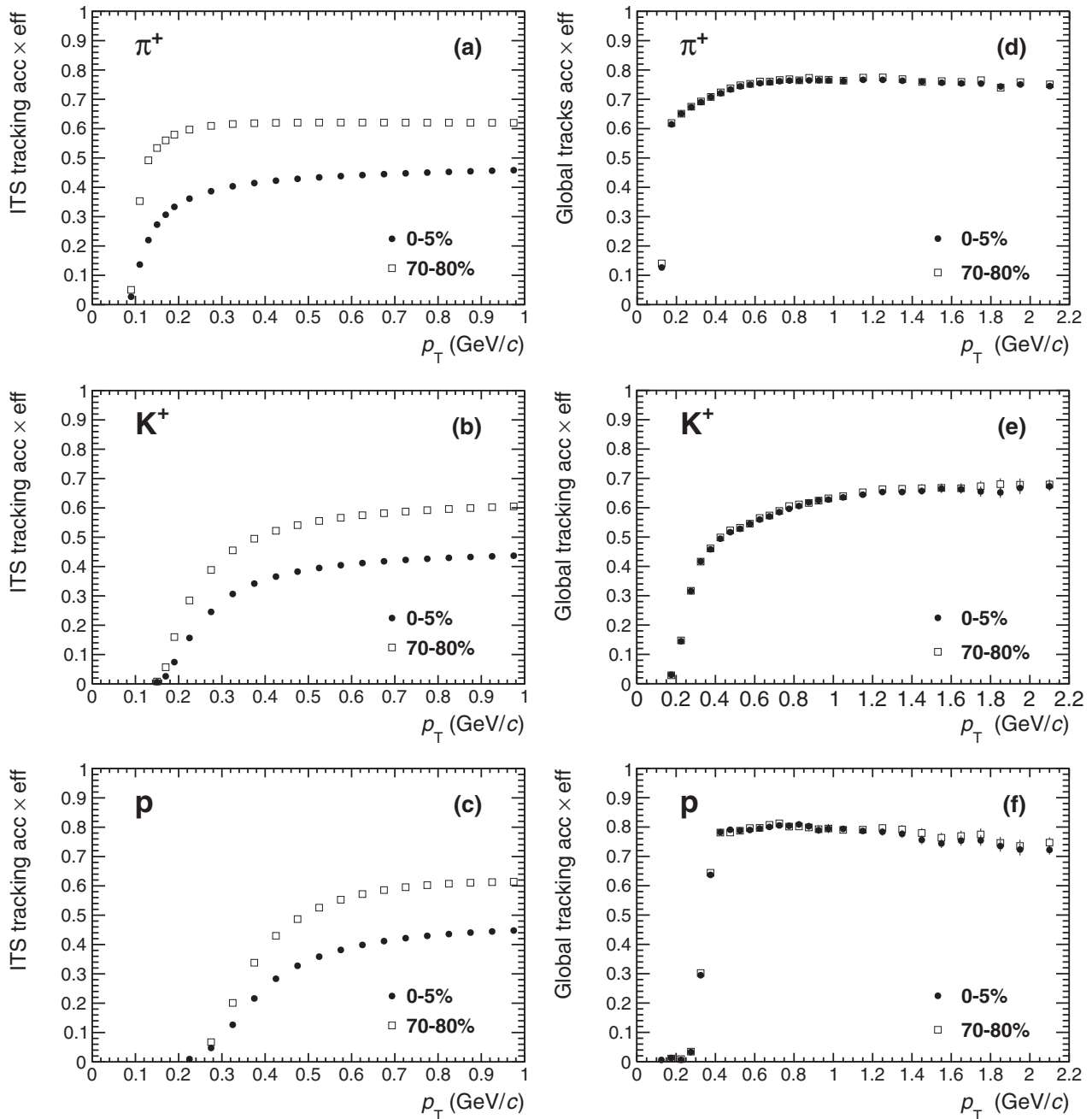
FIG. 1. ITS stand-alone tracking efficiency for (a) pions, (b) kaons, and (c) protons and global tracking efficiency for (d) pions, (e) kaons, and (f) protons in central and peripheral collisions.

TRD. This provides good resolution in the transverse distance of closest approach to the vertex, DCA_{xy}, and, hence, good separation of primary and secondary particles. The track selection required at least 70 clusters in the TPC and at least two points in the ITS, from which at least one must be from the SPD to improve the DCA_{xy} resolution. The tracking efficiency, shown in Figs. 1(d), 1(e), and 1(f), depends only mildly on centrality. It saturates at $\sim$70% because of the inactive channels in the SPD. Simulations with a fully operational ITS show that the intrinsic efficiency of the detector is >90%. The rise of the efficiency at low p_T is due to interactions with the detector material, and it is thus

sharper for protons. The efficiency reaches a maximum when the curvature is big enough for a track to cross the TPC readout chamber boundaries within a relatively small area. In this case, the two track parts can be easily connected (at $p_T \sim 0.6$ GeV/c). The straighter tracks at higher p_T are affected by the geometrical acceptance. This effect is more pronounced for protons than for pions, because the efficiency is folded with the decay probability for pions. While protons are stable particles, there is a nonzero decay probability for pions which decreases towards higher p_T. The shape of the efficiency for kaons, on the other hand, is dominated by the decay probability.
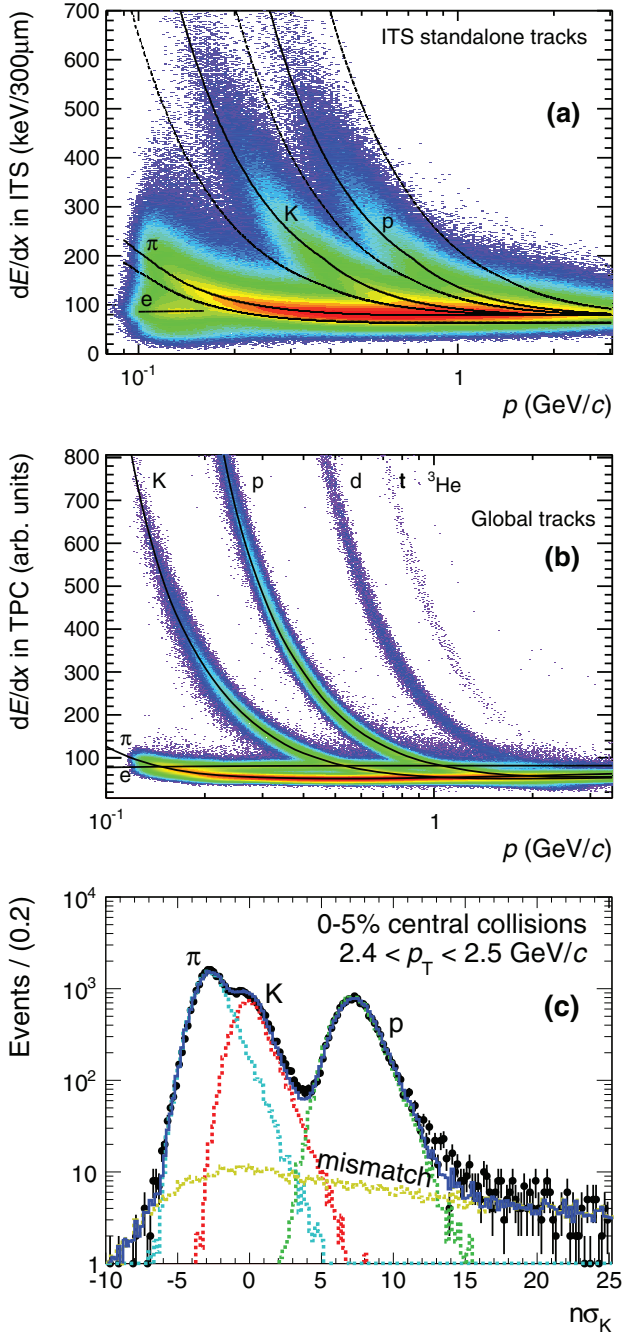
FIG. 2. (Color online) Performance of the PID detectors: (a) dE/dx distribution measured in the ITS: The continuous curves represent the Bethe-Bloch parametrization, the dashed curves the asymmetric bands used in the PID procedure. (b) dE/dx measured in the TPC with global tracks (see text for the definition of global tracks): The continuous curves represent the Bethe-Bloch parametrization. (c) Fit of the TOF time distribution with the expected contributions for negative tracks and for the kaon mass hypothesis in the bin $2.4 < p_T < 2.5$ GeV/c.

The TPC identifies particles via the specific energy loss in the gas: Up to 159 samples can be measured. A truncated mean, utilizing only 60% of the available samples, is employed in the analysis [Fig. 2(b)]. This leads to a Gaussian (and, hence, symmetric) response function, in contrast to the ITS.

The resolution is ~5% in peripheral and ~6.5% in central collisions. Further outwards, the TOF measures the time-of-flight of the particles, allowing identification at higher p_T. The TRD tracking information, if present, is used to constrain the extrapolation to the TOF. The total time resolution is about 85 ps and it is determined by three contributions: the intrinsic timing resolution of the detector and associated electronics, the tracking, and the start time. This makes the identification possible out to $p_T = 3$ GeV/c for pions and kaons and 4.6 GeV/c for protons.

In the intermediate p_T range, track-by-track identification is possible, based on the combined TPC and TOF signals ("TPC/TOF"). It was required that the particles are within 3σ of the expected values measured in the TPC and/or TOF. The TOF information was used starting at $p_T = 0.65$, 0.6, 0.8 GeV/c for π, K, and p, respectively, where the 3σ compatibility cut was required for both TPC and TOF. The additional requirement of a matching TOF hit reduces the overall efficiency shown in Figs. 1(c), 1(d), and 1(e) by about 30%, due to the TOF geometrical acceptance and to the
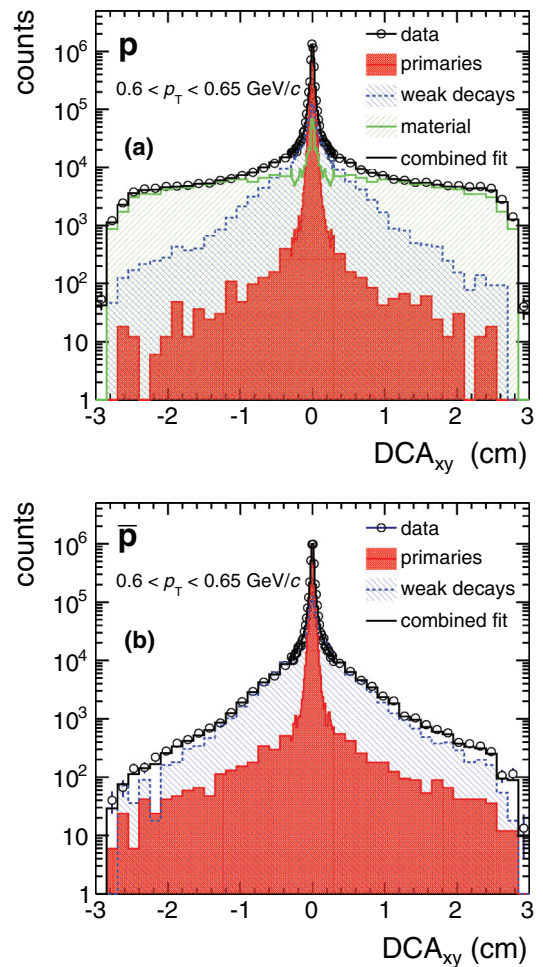

FIG. 3. (Color online) DCA$_{xy}$ of (a) protons and (b) antiprotons in the p_T range between 0.6 GeV/c and 0.65 GeV/c together with the Monte Carlo templates which are fitted to the data (0–5% most central collisions). The dashed areas represent the individual templates and the continuous curve the combined fit.

TABLE II. Main sources of systematic uncertainty.

Effect	$\pi^{\pm}$		$K^{\pm}$		p and $\overline{p}$	
p_T range (GeV/c)	0.1	3	0.2	3	0.35	4.5
Correction for secondaries	1.5%	1%	Negl.		4%	1%
Material budget	5%	Negl.	3%	Negl.	3%	Negl.
Hadronic interactions	2%	1%	4%	1%	6%	1% ($\overline{p}$)
					4%	Negl. (p)
p_T range (GeV/c)	0.1	0.5	0.2	0.5	0.35	0.65
ITS tracking efficiency (central 0–5%)	10%		10%		10%	
ITS tracking efficiency (peripheral 80–90%)	4%		4%		4%	
ITS PID	2%		4%		4.5%	
p_T range (GeV/c)	0.3	0.65	0.3	0.6	0.5	0.8
Global tracking efficiency	4%		4%		4%	
TPC PID (central, 0–5%)	3%		5%		1.5%	
TPC PID (peripheral 80–90%)	1.5%		3.5%		1%	
p_T range (GeV/c)	0.5	3	0.5	3	0.5	4.5
TOF matching efficiency	3%		6%		3%	
TOF PID	2%	7%	3%	15%	5%	25%

additional material (see also Sec. III). The range of this analysis is determined at low p_T by the global tracking efficiency and at high p_T by the contamination from other particle species. Finally, in the third analysis, a statistical identification based on the TOF signal alone was used ("TOF fits"). In order to extend the measurement beyond the region of clear separation, the difference between the measured time-of-flight and the expected one for the particle species under study (normalized to the resolution) was examined. For each p_T bin, this distribution was fitted with the expected shapes (called "templates" in the following) for π, K, and p, allowing the

three particles to be distinguished when the separation is as low as $\sim 2\sigma$. An additional template is needed to account for the tracks which are associated to a wrong hit in the TOF (mismatch). The templates are built from data, using the measured TOF time response function (described by a Gaussian with an exponential tail) and sampling real tracks to get a realistic track-length distribution. This fit was repeated for each mass hypothesis to allow for the calculation of the correct rapidity interval. A worst-case example, for 0–5% central collisions, in the bin $2.4 < p_T < 2.5$ GeV/c and for the kaon mass hypothesis, can be seen in Fig. 2 (bottom).

In this paper, results for "primary" particles are presented, defined as prompt particles produced in the collision, including decay products, except those from weak decays of strange particles. The contamination from secondary particles produced by weak decays or interaction with the material is mostly relevant for (anti-)protons. Since strangeness production is typically underestimated in current event generators, and low p_T interactions with the material are not modeled perfectly in transport codes, the contamination was extracted from data. The transverse DCA_{xy} distribution for selected tracks was fitted with three distributions ("templates" in the following) corresponding to the expected shapes for primary particles and secondaries from material and secondaries from weak decays, as extracted from Monte Carlo. This contribution can reach 35% at $p_T = 300$ MeV/c for protons. An example of DCA_{xy} fits for the bin $0.6 < p_T < 0.65$ GeV/c is shown in Fig. 3: The shapes of the three contributions differ substantially. The distribution corresponding to primary particles reflects the resolution of the DCA_{xy}. The small non-Gaussian tails seen in the figure are mostly due to large-angle scattering [30], tracks with wrongly assigned ITS clusters or to the combination of tracks with hits on the first and/or second ITS layer which have slightly different DCA_{xy} resolution. The secondary particles from weak decays show a wider distribution which reflects the large $c\tau$ of weakly decaying particles (of the order of several centimeters). Finally, the secondaries from material show very flat tails at high DCA_{xy}. The last contribution is negligible in the case of antiprotons. The DCA_{xy} distribution for pions is similar to the one for protons but with much suppressed contribution of secondaries. The distribution for kaons is almost entirely composed of primary particles.

TABLE III. Charged-particle multiplicity density [26] (total uncertainties) and midrapidity particle yields $\frac{dN_i}{dy}|_{|y|<0.5}$ (statistical uncertainties and systematic uncertainties including extrapolation uncertainty). The last column indicates the additional normalization uncertainty coming from the centrality definition.

| Centrality	$dN_{\mathrm{ch}}/d\eta$	π^+	π^-	K^+	K^-	p	$\overline{p}$	Norm. Uncertainty
0–5%	1601 ± 60	733 ± 54	732 ± 52	109 ± 9	109 ± 9	34 ± 3	33 ± 3	0.5%
5–10%	1294 ± 49	606 ± 42	604 ± 42	91 ± 7	90 ± 8	28 ± 2	28 ± 2	0.5%
10–20%	966 ± 37	455 ± 31	453 ± 31	68 ± 5	68 ± 6	21.0 ± 1.7	21.1 ± 1.8	0.7%
20–30%	649 ± 23	307 ± 20	306 ± 20	46 ± 4	46 ± 4	14.4 ± 1.2	14.5 ± 1.2	1%
30–40%	426 ± 15	201 ± 13	200 ± 13	30 ± 2	30 ± 2	9.6 ± 0.8	9.7 ± 0.8	2%
40–50%	261 ± 9	124 ± 8	123 ± 8	18.3 ± 1.4	18.1 ± 1.5	6.1 ± 0.5	6.2 ± 0.5	2.4%
50–60%	149 ± 6	71 ± 5	71 ± 4	10.2 ± 0.8	10.2 ± 0.8	3.6 ± 0.3	3.7 ± 0.3	3.5%
60–70%	76 ± 4	37 ± 2	37 ± 2	5.1 ± 0.4	5.1 ± 0.4	1.9 ± 0.2	2.0 ± 0.2	5%
70–80%	35 ± 2	17.1 ± 1.1	17.0 ± 1.1	2.3 ± 0.2	2.3 ± 0.2	0.90 ± 0.08	0.93 ± 0.09	6.7%
80–90%	$13.4 + 1.6 - 1.2$	6.6 ± 0.4	6.6 ± 0.4	0.85 ± 0.08	0.86 ± 0.09	0.36 ± 0.04	0.36 ± 0.04	$+12\% -8.5\%$
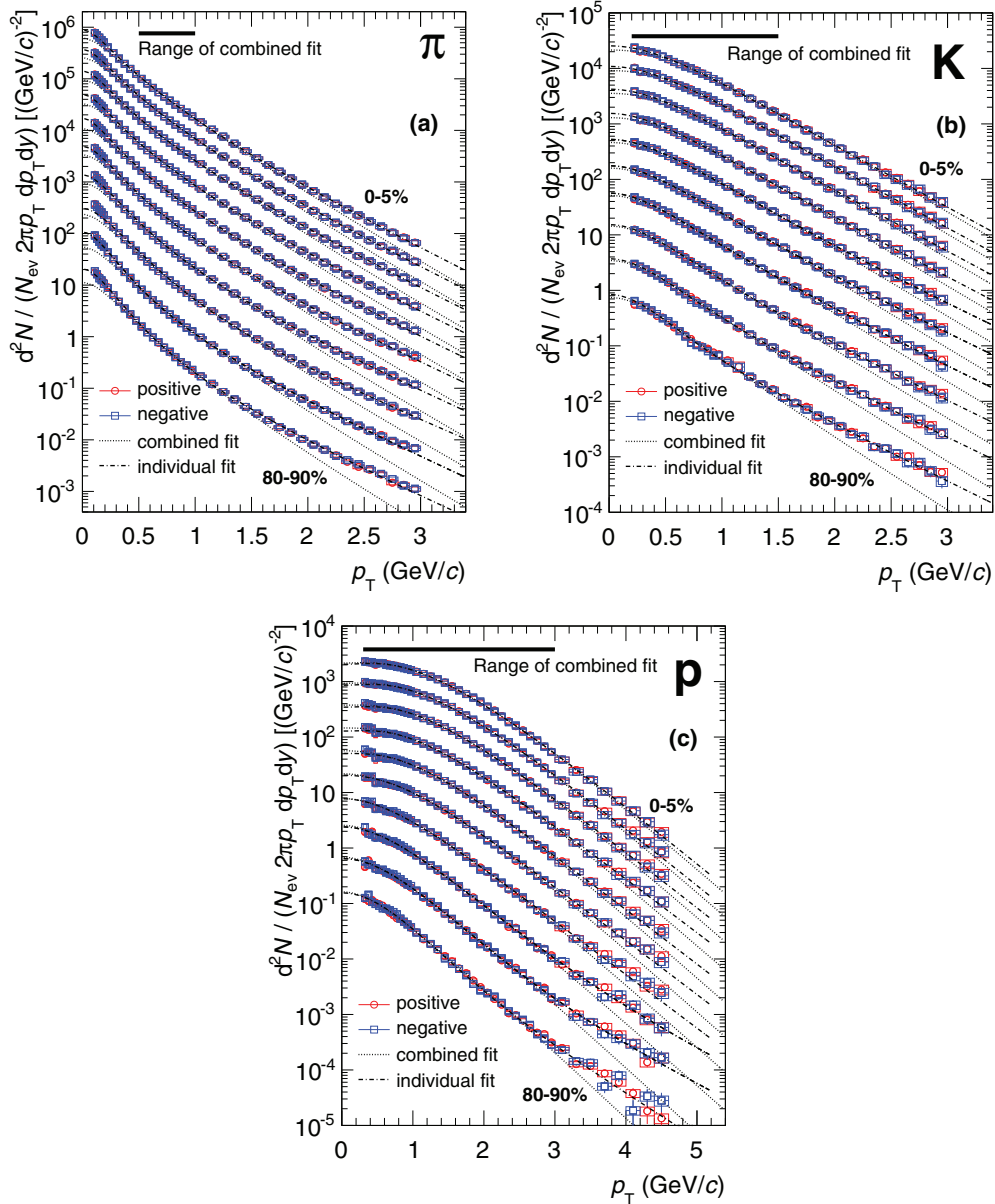
FIG. 4. (Color online) Transverse-momentum (p_T) distribution of (a) π, (b) K, and (c) p as a function of centrality, for positive (circles) and negative (squares) hadrons. Each panel shows central to peripheral data; spectra scaled by factors 2^n (peripheral data not scaled). Dashed curves: blast-wave fits to individual particles; dotted curves: combined blast-wave fits (see text for details). Statistical (error bars) and systematic (boxes) uncertainties plotted. An additional normalization uncertainty (Table III) has to be added in quadrature.

The efficiency correction and the templates used in the secondary correction procedure were computed with about 1 million Monte Carlo events, generated using the HIJING [31] event generator, tuned to reproduce approximately the $dN_{\mathrm{ch}}/d\eta$ as measured for central collisions [27]. The transport of particles through the detector was simulated using GEANT3 [32]. The results of the three analyses were combined using the (largely independent) systematic uncertainties as weights in the overlapping ranges, after checking for their compatibility.

III. SYSTEMATIC UNCERTAINTIES

Several effects related to the transport of particles through the detector and support materials contribute to the systematic

uncertainties, namely (i) the amount of secondary protons which are produced in the material, (ii) corrections for energy loss through electromagnetic interactions, and (iii) absorption of antimatter due to hadronic interactions. The first effect is taken into account in the data-driven DCA_{xy} fit procedure, and its uncertainties are estimated with the DCA_{xy} fit variations discussed below. The uncertainties due to the second effect were estimated varying the material budget in the simulation by $\pm 7\%$ and are of the order of 3% and 1% for pions and kaons and 5% and 2% for protons in the two lowest p_T bins, respectively, and then quickly decrease further, becoming negligible towards higher momenta. In order to account for the last effect, different transport codes (GEANT3, GEANT4 [33],

and FLUKA [34]) were compared. GEANT3 (the default transport code used in this work) is known not to reproduce the cross sections relevant for the interactions with the material at low p_T [35]. The efficiencies were scaled with a factor computed with a dedicated FLUKA [35] simulation. This allows the uncertainty for antiprotons to be limited to <6% despite the

large absorption cross section, as there are sufficient existing data on $\bar{p}$ nucleus collisions to validate the transport codes. A detailed comparison of GEANT3 with the few existing measurements of hadronic interaction cross sections of low momentum kaons and pions [36–40] reveals differences of about 20–30%. After folding with the relevant percentage of particles which are lost due to hadronic interaction before entering the TPC or the TOF, the resulting uncertainty is of the order of 2–3% for K^- and π and below 1% for K^+.

Uncertainties in the estimate of contamination from secondary particles can arise from differences in the DCA_{xy}
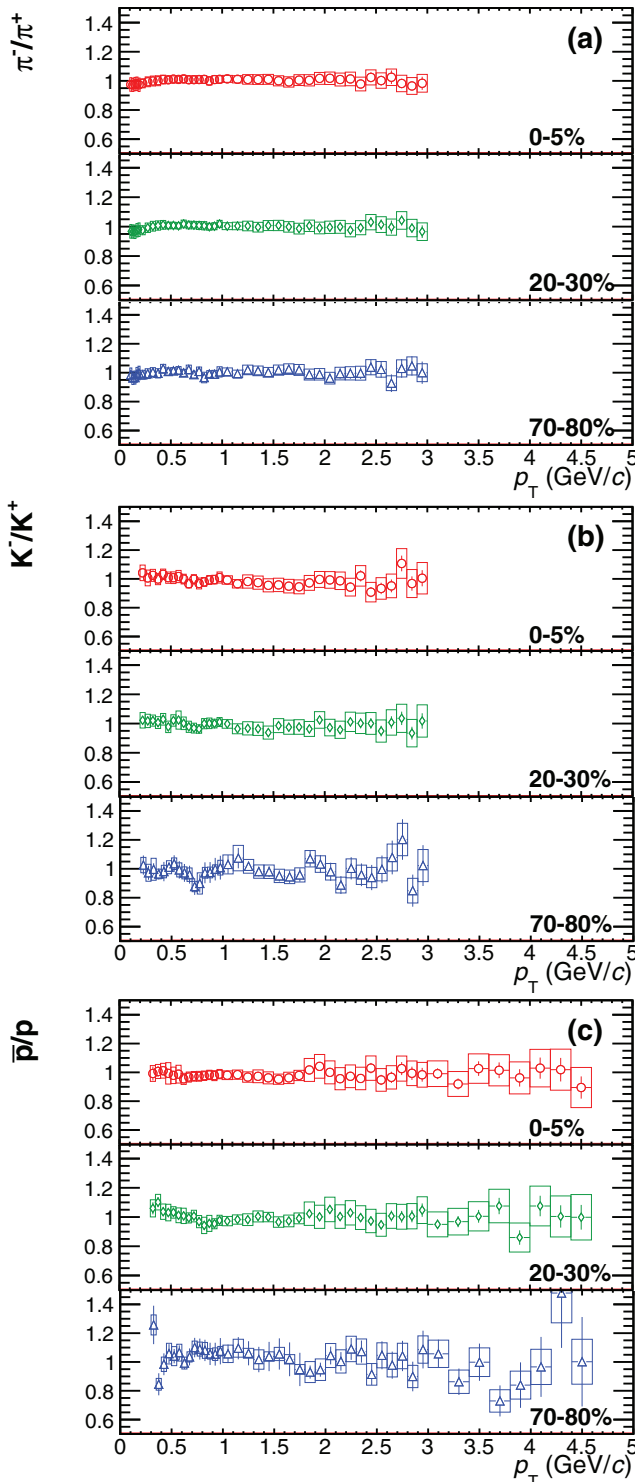
FIG. 5. (Color online) (a) π^-/π^+, (b) K^-/K^+, and (c) $\bar{p}/p$ ratios as a function of p_T for central, semicentral, and peripheral events.
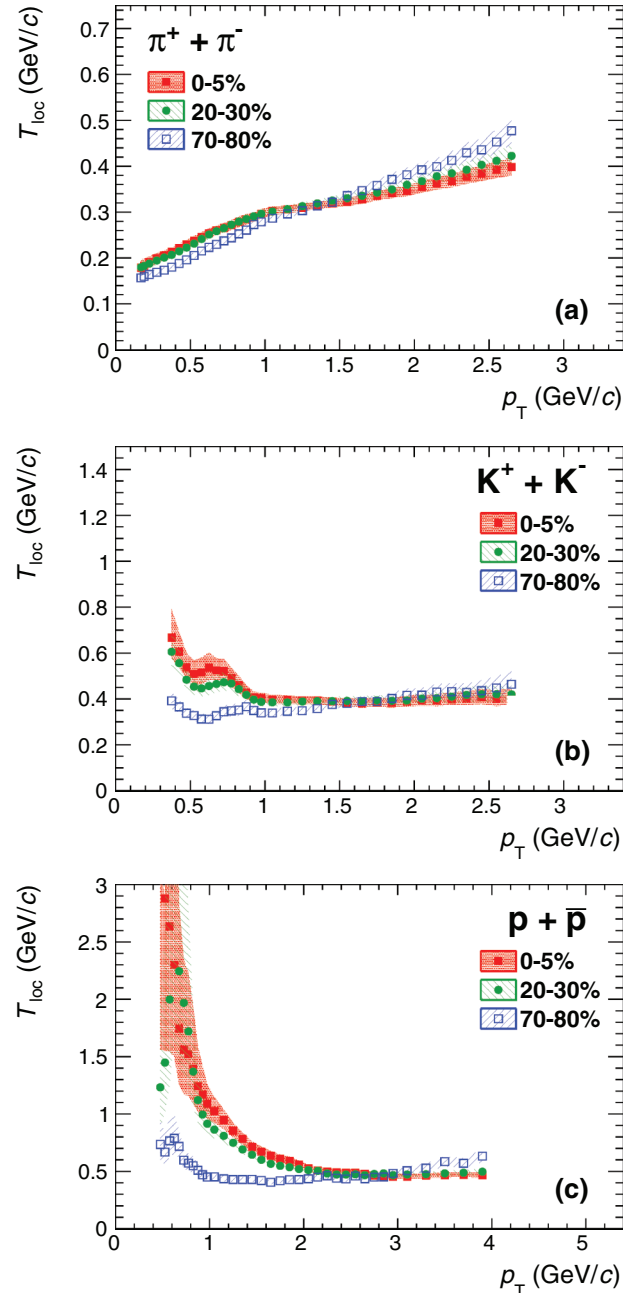
FIG. 6. (Color online) Local slopes of the p_T distributions of (a) π, (b) K, and (c) p (summed charge states) as a function of p_T and centrality. See text for details.

distributions between data and Monte Carlo. In particular, the DCA_{xy} distribution for secondary particles coming from weak decays is affected by the $c\tau$ of the decaying mother and the actual template used in the fits is a mixture of contributions from different particles. The uncertainties due to the secondary subtraction procedure were estimated for all analyses by varying the range of the DCA_{xy} fit, by using different track selections (for instance, using TPC-only tracks), by applying different cuts on the (longitudinal) DCA_z, and by varying the particle composition of the Monte Carlo templates used in the fit. Overall, the effect is of the order of 3% to 1% for pions and 4% to 1% for protons. Such an uncertainty is not relevant for kaons, which have a negligible contamination from secondary particles. Moreover the agreement between the ITS stand-alone and the TPC analyses provides an additional cross-check of this procedure, because different tracking methods have different sensitivity to contamination from secondaries.

At the lowest p_T, the main contribution to the systematic uncertainties comes from the ITS stand-alone tracking efficiency, due to the small number of tracking points and the strong centrality dependence. The uncertainty was estimated using the global tracking as a reference. For each reconstructed global track, a corresponding ITS stand-alone track is sought in a narrow window defined as $\Delta\eta < 0.03$, $\Delta\phi < 0.03$, and $\Delta p_T < 0.1 \times p_T$. If a track is found, the ITS stand-alone tracking is considered efficient. This pseudoefficiency is then compared in data and Monte Carlo to extract the corresponding systematic uncertainty, estimated to be about 10% for central and 3% for peripheral collisions. The efficiency of the ITS stand-alone reconstruction depends strongly on centrality (Fig. 1, left), so a careful matching between the multiplicity in data and Monte Carlo is important. As mentioned, the simulation was adjusted to reproduce the $dN_{ch}/d\eta$ measured for central collisions. The occupancy of all ITS layers and the reconstructed track multiplicity were compared between data and Monte Carlo. Residual differences, due to the different dependence of multiplicity on centrality in data and Monte Carlo, contribute to the systematic uncertainty on the tracking mentioned above and are of the order 2%. The sensitivity to the variation of the track selection cuts (DCA_{xy}, χ^2, number of clusters) was found to be of the order of 7% for all particles. Moreover, the Lorentz force causes shifts of the cluster position in the ITS, pushing the charge in opposite directions when

switching the polarity of the magnetic field of the experiment (E×B effect). This effect is not fully reproduced in the Monte Carlo simulation and was estimated analyzing data samples collected with different magnetic field polarities. This uncertainty is relevant only at the lowest p_T and is 3% for pions and 1% for kaons and protons.

The uncertainties related to the ITS PID method were estimated by using different techniques for the identification. A 3σ cut on the maximum difference in energy loss of the particles was applied (instead of using all particles as in the default strategy). Alternatively, an unfolding method was used, in which, for each p_T bin, the dE/dx distribution is fitted with Monte Carlo templates for each one of the species, similarly to what is done in the TOF fits. The effect is found to be 2%, 4%, and 7% for π, K, and p, respectively. Close to the high-p_T boundaries of the analyses (Table I), the possibility of misidentifying other species is not completely negligible. This is corrected for with Monte Carlo, and the corresponding uncertainty, due to residual differences in particle ratios and dE/dx between data and Monte Carlo is estimated to be 2% for kaons and 1% for protons.

The uncertainty in the global tracking efficiency was estimated comparing the track matching efficiency from TPC to ITS and from ITS to TPC in data and Monte Carlo. The effect is found to be $\sim$4%. The uncertainties related to the track selection were investigated by a variation of the track cuts. They are estimated (for most central collisions) to be 3% for pions and kaons and 4% for protons. This uncertainty decreases slightly for peripheral collisions. The uncertainties related to the TPC/TOF PID procedure were estimated varying the PID cut between 2 and 5 σ. As pions are the most abundant particles, their corresponding systematic uncertainty does not exceed 3% even in regions where the mean pion energy loss crosses the kaon and proton curves. On the other hand, it can reach up to 4–5% for kaons. The corresponding systematics of the better separated protons are below 1.5%. As the dE/dx resolution becomes slightly worse with increasing multiplicity, the systematic uncertainty shows a similar slight increase. The values quoted here represent upper bounds for all centralities as they correspond to the 0–5% most central collisions.

The uncertainties on the response functions of the PID detectors were found to have a negligible effect: They were carefully tuned using high-statistics data and this analysis is

TABLE IV. $\langle p_T \rangle$ as a function of centrality (GeV/c), statistical uncertainties and systematic uncertainties including extrapolation uncertainty summed in quadrature (systematic uncertainties dominate).

Centrality	π^+	π^-	K^+	K^-	p	$\overline{p}$
0–5%	0.517 ± 0.019	0.520 ± 0.018	0.876 ± 0.026	0.867 ± 0.027	1.333 ± 0.033	1.353 ± 0.034
5–10%	0.517 ± 0.018	0.521 ± 0.017	0.872 ± 0.025	0.866 ± 0.028	1.324 ± 0.033	1.344 ± 0.033
10–20%	0.517 ± 0.017	0.521 ± 0.017	0.871 ± 0.027	0.864 ± 0.030	1.311 ± 0.034	1.325 ± 0.036
20–30%	0.512 ± 0.017	0.516 ± 0.017	0.860 ± 0.029	0.851 ± 0.034	1.281 ± 0.033	1.295 ± 0.039
30–40%	0.504 ± 0.017	0.507 ± 0.017	0.842 ± 0.032	0.831 ± 0.031	1.237 ± 0.032	1.243 ± 0.041
40–50%	0.492 ± 0.017	0.497 ± 0.018	0.818 ± 0.030	0.808 ± 0.028	1.178 ± 0.030	1.182 ± 0.033
50–60%	0.478 ± 0.017	0.483 ± 0.017	0.790 ± 0.028	0.775 ± 0.027	1.118 ± 0.028	1.107 ± 0.032
60–70%	0.465 ± 0.017	0.470 ± 0.016	0.760 ± 0.028	0.754 ± 0.027	1.050 ± 0.027	1.045 ± 0.039
70–80%	0.452 ± 0.017	0.455 ± 0.017	0.737 ± 0.027	0.733 ± 0.028	0.987 ± 0.025	0.981 ± 0.031
80–90%	0.434 ± 0.014	0.439 ± 0.017	0.711 ± 0.027	0.692 ± 0.026	0.905 ± 0.026	0.890 ± 0.035

limited to regions where the separation of different particles is $\gtrsim 2\sigma$.

As mentioned above, the tracks reaching the TOF detector have to cross a substantial amount of additional material budget (about $23\% X/X_0$), mostly from the Transition Radiation Detector (TRD) [24]. The systematic uncertainties on the TOF matching were estimated comparing the matching efficiency evaluated in Monte Carlo and from data using samples of cleanly identified particles in TPC. Good agreement is observed in case of pions and kaons, with deviations at the

level of at most 3% and 6%, respectively, over the full p_T range.

In the case of protons and antiprotons good agreement is also observed, for $p_T > 1$ GeV/c, with maximal deviations of 7.5%. Since the TRD was not fully installed in 2010, the analysis was repeated for regions in azimuth with and without installed TRD modules, allowing to cross-check the uncertainty on the material. The effect is found to be 3%, 6%, and 3% for π, K, and p, respectively. The uncertainties related to the identification in the "TOF fits" analysis were estimated varying the parameters of the expected sources in the fit
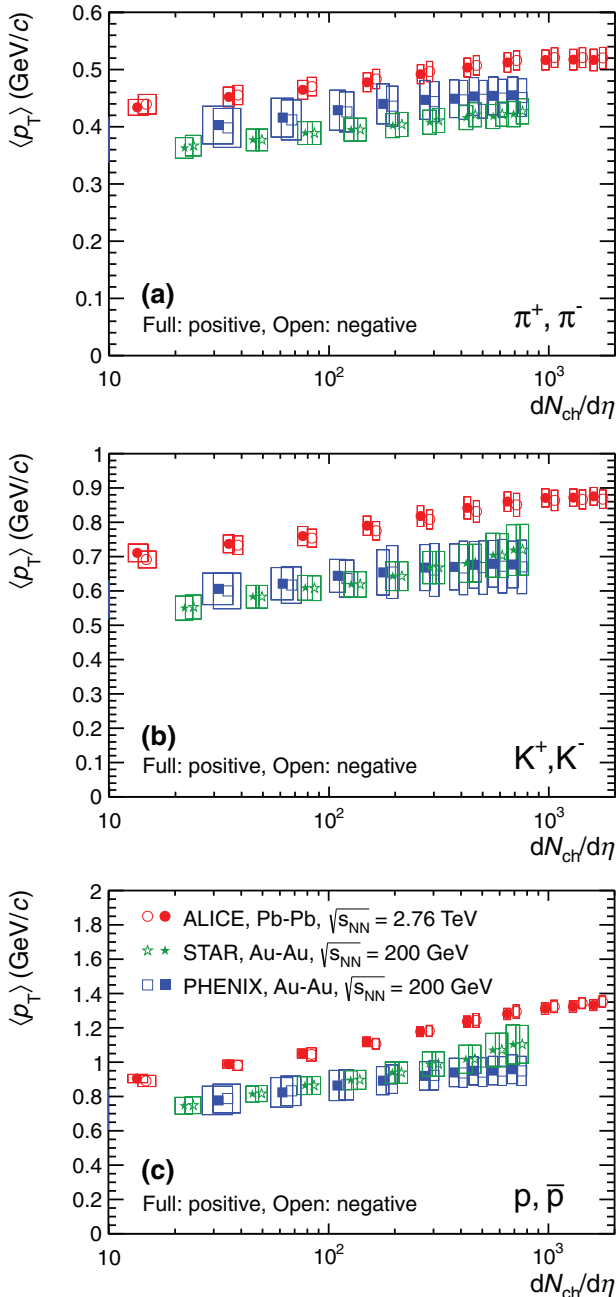
FIG. 7. (Color online) Mean transverse momentum $\langle p_T \rangle$ as a function of $dN_{\mathrm{ch}}/d\eta$ for (a) π, (b) K, and (c) p compared to RHIC results at $\sqrt{s_{NN}} = 200$ GeV [42,45]. Negative charge results displaced for better readability. Boxes: systematic uncertainties.
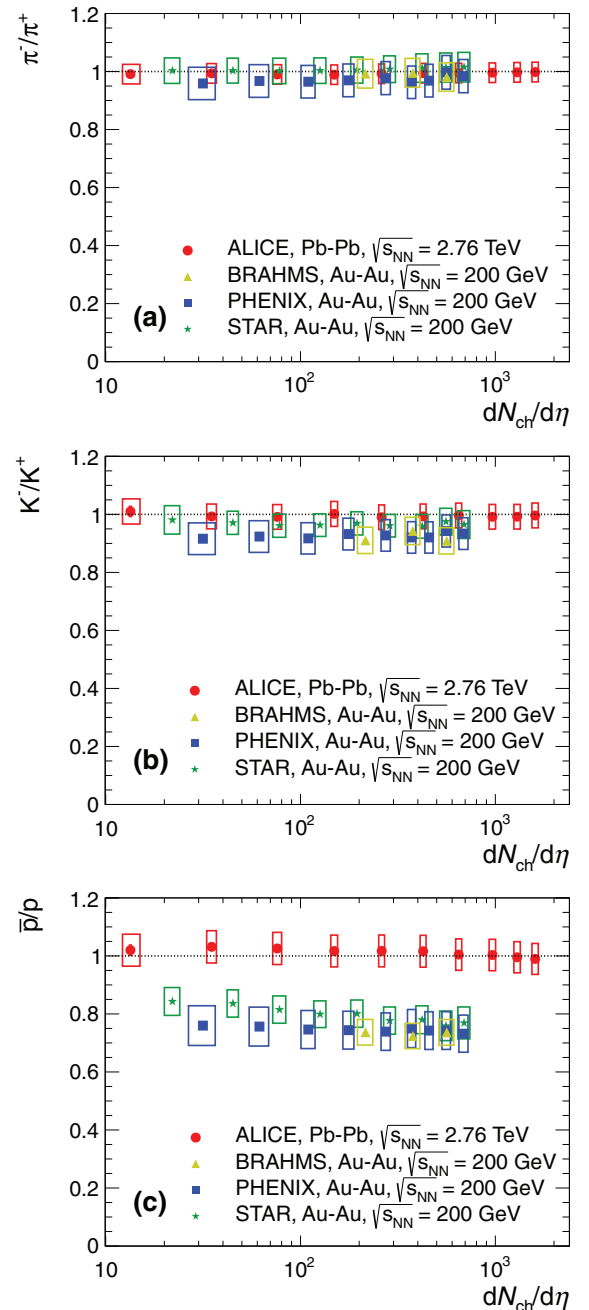
FIG. 8. (Color online) (a) π^-/π^+, (b) K^-/K^+, and (c) $\bar{p}/p$ ratios as a function of $dN_{\mathrm{ch}}/d\eta$, compared to previous results at $\sqrt{s_{NN}} = 200$ GeV.

by $\pm 10\%$. This is one of the main sources of uncertainty and increases with p_T, as the separation between different species decreases. It is $<5\%$ at $p_T \sim 0.5$ GeV/c and $\lesssim 7\%$, 15%, 25% at high p_T for π, K, and p, respectively. The main sources of systematic uncertainties are summarized in Table II.

The measured spectra are further affected by an additional normalization uncertainty, coming from the centrality estimation. The centrality percentiles are determined with sharp cuts on the VZERO amplitude distribution, which are affected by a 1% uncertainty [25]. This translates into a normalization uncertainty on the spectra. The total normalization uncertainty is about $+12\%$ -8.5% for peripheral events (also including a 6% contribution due to contamination from electromagnetic processes) and negligible for central events; see Table III.

IV. RESULTS

A. Transverse-momentum distributions

The combined spectra in the centrality bins reported in Table III are shown in Fig. 4. The distributions of positive and negative particles are compatible within uncertainties at all p_T, as expected at LHC energies. This is clearly seen in the ratio of negative to positive p_T spectra shown in Fig. 5. For this reason, we focus in the following mostly on results for combined charges.
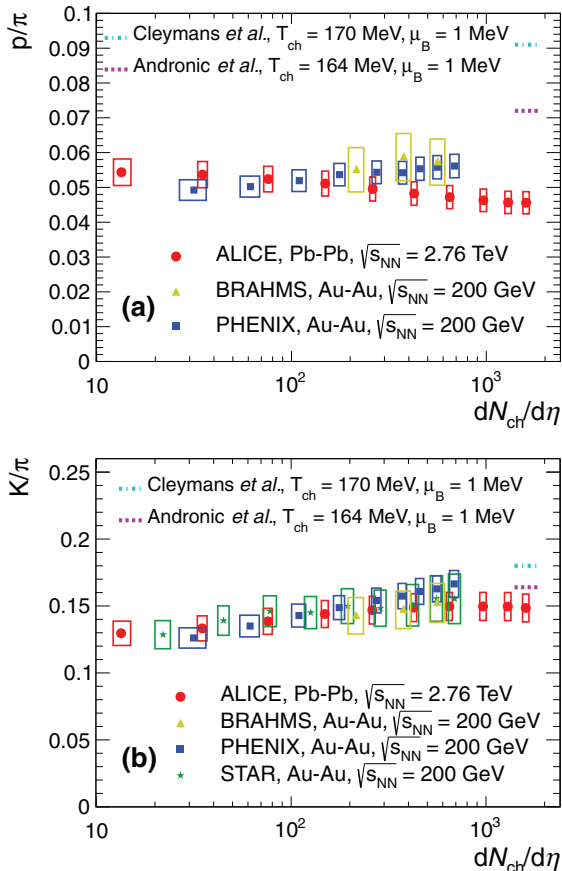
FIG. 9. (Color online) (a) $p/\pi = (p + \bar{p})/(\pi^+ + \pi^-)$ and (b) $K/\pi = (K^+ + K^-)/(\pi^+ + \pi^-)$ ratios as a function of $dN_{ch}/d\eta$, compared to previous results at $\sqrt{s_{NN}} = 200$ GeV.

The change of shapes with centrality is apparent in Fig. 4: the spectra get harder with increasing centrality. The spectra for all particle species have an almost exponential shape at high p_T in central collisions: Contrary to what is observed in pp collisions [22], there is no obvious onset of a high-p_T power-law tail. In more peripheral collisions, the onset of the power law is visible at high p_T. This is quantified in Fig. 6 which shows the local inverse slope T_{loc} of the spectra, as a function of p_T, computed with a fit using five bins in the vicinity of each p_T bin with the function

$$\frac{1}{p_T}\frac{dN}{dp_T} \propto e^{-p_T/T_{loc}}. \tag{1}$$

This approach guarantees a numerically stable extraction of the local inverse slope parameter T_{loc} but leads to a significant correlation of the depicted uncertainties for neighboring points. Residual correlations in the bin-by-bin systematics artificially increase the uncertainties on T_{loc} shown in Fig. 6. As seen in the figure, the inverse slopes of K and p become larger with decreasing p_T (the spectra are flatter at low p_T), and this change is more pronounced for central collisions. The proton spectrum at low p_T is nearly flat, making T_{loc} unconstrained (for a flat distribution, $T_{loc} \to \infty$). Above a certain p_T, roughly 1 GeV/c for K and 2 GeV/c for p, the slopes do not change with p_T for central and semicentral collisions, consistent with an exponential shape. Protons and kaons converge to similar values of $T_{loc} \sim 0.45$ GeV/c. For peripheral collisions, a modest increase of T_{loc} is seen at the highest p_T, suggesting the onset of a power-law behavior. The T_{loc} trend differs for pions. The π spectra are not purely exponential. At high-p_T the power-law rise is more suppressed in central collisions compared to peripheral ones. At low p_T T_{loc} increases with p_T, opposite to the trend observed for protons and kaons. This steepening of the pion spectra is a general feature of heavy-ion collisions and is due to the large contribution of resonance decays to the pion spectrum, as already noted in Refs. [9,41]. Above $p_T \simeq 1$ GeV/c, the rate of increase of T_{loc} is slower than at lower p_T and is less pronounced for central collisions.

B. p_T-integrated yields and mean transverse momentum

In order to extrapolate to zero p_T for the extraction of p_T-integrated yields and $\langle p_T \rangle$, the spectra were fitted individually with a blast-wave function [9] as follows:

$$\frac{1}{p_T}\frac{dN}{dp_T} \propto \int_0^R r\,dr\,m_T\,I_0\left(\frac{p_T \sinh\rho}{T_{kin}}\right)K_1\left(\frac{m_T \cosh\rho}{T_{kin}}\right), \tag{2}$$

where the velocity profile ρ is described by

$$\rho = \tanh^{-1}\beta_T = \tanh^{-1}\left(\left(\frac{r}{R}\right)^n \beta_s\right). \tag{3}$$

Here, $m_T = \sqrt{p_T^2 + m^2}$ is the transverse mass, I_0 and K_1 are the modified Bessel functions, r is the radial distance in the transverse plane, R is the radius of the fireball, β_T is the transverse expansion velocity, and β_s is the transverse expansion velocity at the surface. From these equations one can also derive the average transverse expansion velocity $\langle \beta_T \rangle$.

TABLE V. Results of the combined blast-wave fits, in the default ranges 0.5–1 GeV/c, 0.2–1.5 GeV/c, and 0.3–3 GeV/c for π, K, and p, respectively. The first uncertainty in the table includes the effect of the bin-by-bin systematic uncertainties and the second is the full systematic uncertainty. See text for details.

Centrality	$\langle \beta_T \rangle$	T_{kin} (GeV/c)	n	χ^2/n_{DOF}
0–5%	$0.651 \pm 0.004 \pm 0.020$	$0.095 \pm 0.004 \pm 0.010$	$0.712 \pm 0.019 \pm 0.086$	0.15
5–10%	$0.646 \pm 0.004 \pm 0.023$	$0.097 \pm 0.003 \pm 0.011$	$0.723 \pm 0.019 \pm 0.116$	0.20
10–20%	$0.639 \pm 0.004 \pm 0.022$	$0.099 \pm 0.004 \pm 0.011$	$0.738 \pm 0.020 \pm 0.118$	0.19
20–30%	$0.625 \pm 0.004 \pm 0.025$	$0.101 \pm 0.004 \pm 0.012$	$0.779 \pm 0.022 \pm 0.133$	0.22
30–40%	$0.604 \pm 0.005 \pm 0.022$	$0.106 \pm 0.004 \pm 0.012$	$0.841 \pm 0.025 \pm 0.168$	0.22
40–50%	$0.574 \pm 0.005 \pm 0.016$	$0.112 \pm 0.004 \pm 0.013$	$0.944 \pm 0.029 \pm 0.142$	0.22
50–60%	$0.535 \pm 0.007 \pm 0.018$	$0.118 \pm 0.004 \pm 0.014$	$1.099 \pm 0.038 \pm 0.187$	0.28
60–70%	$0.489 \pm 0.008 \pm 0.024$	$0.129 \pm 0.005 \pm 0.017$	$1.292 \pm 0.052 \pm 0.194$	0.36
70–80%	$0.438 \pm 0.011 \pm 0.039$	$0.139 \pm 0.005 \pm 0.027$	$1.578 \pm 0.081 \pm 0.205$	0.40
80–90%	$0.357 \pm 0.016 \pm 0.084$	$0.151 \pm 0.006 \pm 0.044$	$2.262 \pm 0.191 \pm 0.498$	0.52

The free parameters in the fit are the freeze-out temperature T_{kin}, the average transverse velocity $\langle \beta_T \rangle$, and the exponent of the velocity profile n. This function describes very well all particle species over the whole measured p_T range (as individual fits). It should be noted, however, that from fits to a single-particle species no physics meaning can be attached to those parameters. A combined fit to different particle species can provide insight on the freeze-out parameters, and this is discussed in detail in the next section. The fraction of extrapolated yield is small: about 7%, 6%, and 4% for π, K, and p, respectively. The systematic uncertainties due to the extrapolation amounts to 2.5%, 3%, and 3% for the yields and to 2%, 1%, and 1% for $\langle p_T \rangle$ (independent of centrality). This was estimated using different fit functions [42] (Boltzmann, m_T exponential, p_T exponential, Tsallis-Levy, Fermi-Dirac, and Bose-Einstein), restricting the fit range to low p_T for those functions not giving a satisfactory description of the spectra over the full range. The $\langle p_T \rangle$ is computed extrapolating with the blast wave function to 100 GeV/c (infinity, effectively). The difference between the $\langle p_T \rangle$ computed with and without the extrapolation at high p_T is <1%, ∼1.5%, and <1% for π, K, and p, respectively. The extracted particle yields and $\langle p_T \rangle$ as a function of centrality are summarized in Table III and Table IV.

Figure 7 shows the mean transverse momentum $\langle p_T \rangle$ as a function of $dN_{ch}/d\eta$, compared to previous results at RHIC[1] [42,43,45]. The $\langle p_T \rangle$ increases with centrality and is higher

<hr/>

[1]The RHIC data are plotted as a function of $dN_{ch}/d\eta$ using the measured $dN_{ch}/d\eta$ of each individual experiment [42–44]. In the case of PHENIX, the $dN_{ch}/d\eta$ are published in 5% percentiles, while the spectra are published mostly in 10% percentiles: whenever needed, the value of the $dN_{ch}/d\eta$ used in the figure is a linear interpolation of the 5% percentiles; the $dN_{ch}/d\eta$ measurement, moreover, is only available up to 70% centrality in PHENIX. Since there is some disagreement in the $dN_{ch}/d\eta$ measurements from different RHIC experiments for peripheral event, we decided not to plot in Fig. 7 the PHENIX results below 70% centrality. The discrepancy is also visible in Fig. 15, where the difference in normalization between STAR and PHENIX is apparent. The STAR (anti-)proton measurement is inclusive of products from weak decays of strange particles and therefore not included in all comparisons shown in this section.

than the lower-energy results for comparable charged-particle densities. The $\langle p_T \rangle$ at RHIC was found to be compatible with a scaling as a function of $dN_{ch}/d\eta$ for different energies [42]. This scaling is clearly excluded at the LHC.

The ratios of negative to positive particle yields (Fig. 8) are compatible with unity for all centralities. The $\bar{p}/p$ ratio, in particular, confirms the expectation of a vanishing baryon transport to midrapidity at the LHC, in contrast to to the RHIC energy regime, where the $\bar{p}/p$ ratio was found to be about 0.8 at $\sqrt{s_{NN}} = 200$ GeV [42]. The effect of the different antibaryon-to-baryon asymmetry between the two energies is almost absent in the sum of the positive and negative charges. Therefore, the ratios $K/\pi = (K^+ + K^-)/(\pi^+ + \pi^-)$ and $p/\pi = (p + \bar{p})/(\pi^+ + \pi^-)$ are compared to RHIC [42,44,45] in Fig. 9 as a function of charged-particle multiplicity. The K/π ratio hints at a small increase with centrality following the trend from lower-energy data. The p/π ratio suggests a small decrease with centrality and is slightly lower than the RHIC measurements.

V. DISCUSSION

A. Transverse-momentum distributions and hydrodynamics

The change with centrality of the spectral shapes shown in Fig. 4 and Fig. 6 can be interpreted in terms of hydrodynamics. A flattening of the spectra, more pronounced at low p_T and for heavier particles, is expected in the hydrodynamical models as a consequence of the blue-shift induced by the collective expansion. The low-p_T change of the local slope shown in Fig. 6, more pronounced for the proton spectra, thus suggests a progressively stronger radial flow with increasing centrality. The fact that the inverse slope converges to the same value for p and K at high p_T is also a generic feature of the blast-wave parametrization.

In order to quantify the freeze-out parameters at $\sqrt{s_{NN}} = 2.76$ TeV, a combined fit of the spectra with the blast-wave function Eq. (2) was performed in the ranges 0.5–1 GeV/c, 0.2–1.5 GeV/c, and 0.3–3 GeV/c for π, K, and p, respectively. The pions at low p_T are known to have a large contribution from resonance decays, while at high p_T a hard contribution (not expected to be described by the blast wave)
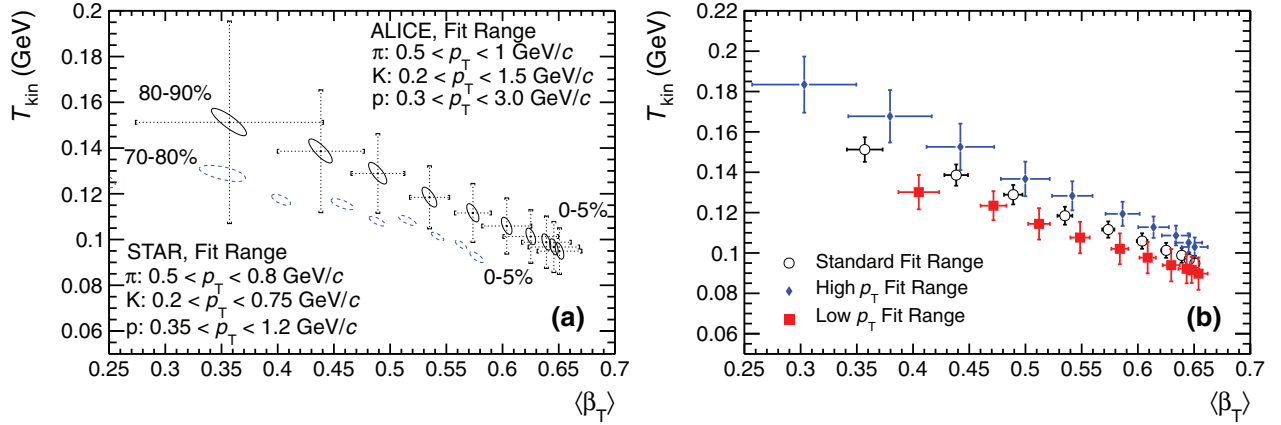
FIG. 10. (Color online) (a) Results of blast-wave fits compared to similar fits at RHIC energies [5]. The uncertainty contours include the effect of the bin-by-bin systematic uncertainties, the dashed error bars represents the full systematic uncertainty (see text for details), and the STAR contours include only statistical uncertainties. (b) Comparison of fit results for different fit ranges; the error bars include only the effect of the bin-by-bin systematics (see text for details).

may set in. Therefore, the values of the parameters extracted from the fit, and especially T_{kin}, are sensitive to the fit range used for the pions. Forcing all species to decouple with the same parameters also makes the interpretation of the results arguable: different particles can in principle decouple at a different time, and, hence, with a different $\langle \beta_T \rangle$ and T_{kin}, from the hadronic medium, due to their different hadronic cross section. These fits by no means replace a full hydrodynamical calculation: Their usefulness lies in the ability to compare with a few simple parameters the measurements at different $\sqrt{s_{NN}}$. As will be discussed, the parameters extracted from such a combined fit depend on the range used for the different particles. Our standard fit ranges were therefore chosen to be similar to the ones used by the STAR collaboration at $\sqrt{s_{NN}} = 200$ GeV/c at the low p_T end. The high p_T boundaries were extended to higher p_T as compared to STAR, since at the LHC it is expected that the shapes are dominated by collective effects out to higher transverse momenta. The results of the fit are summarized in Table V and shown in Fig. 10(a) and in Fig. 11. The 1σ uncertainty ellipses shown in

the figure reflect the bin-to-bin systematic uncertainties. The uncertainties shown as dashed bars and reported in Table V also include systematic uncertainties related to the stability of the fit: The effect of the variation of the lower fit bound for pions (to test the effect of resonance feed-down) and the sensitivity to different particle species (i.e., excluding pions or kaons or protons) and to fits to the individual analyses. The value of $\langle \beta_T \rangle$ extracted from the fit increases with centrality, while T_{kin} decreases, similar to what was observed at lower energies (Figs. 10 and 11 and Table V). This was interpreted as a possible indication of a more rapid expansion with increasing centrality [5]. In peripheral collisions this is consistent with the expectation of a shorter lived fireball with stronger radial gradients [10].

The value of the n parameter, Eq. (3), is about 0.7 in central collisions and it increases towards peripheral collisions. The large values in peripheral collisions are likely due to the spectrum not being thermal over the full range: The n parameter increases to reproduce the power-law tail.
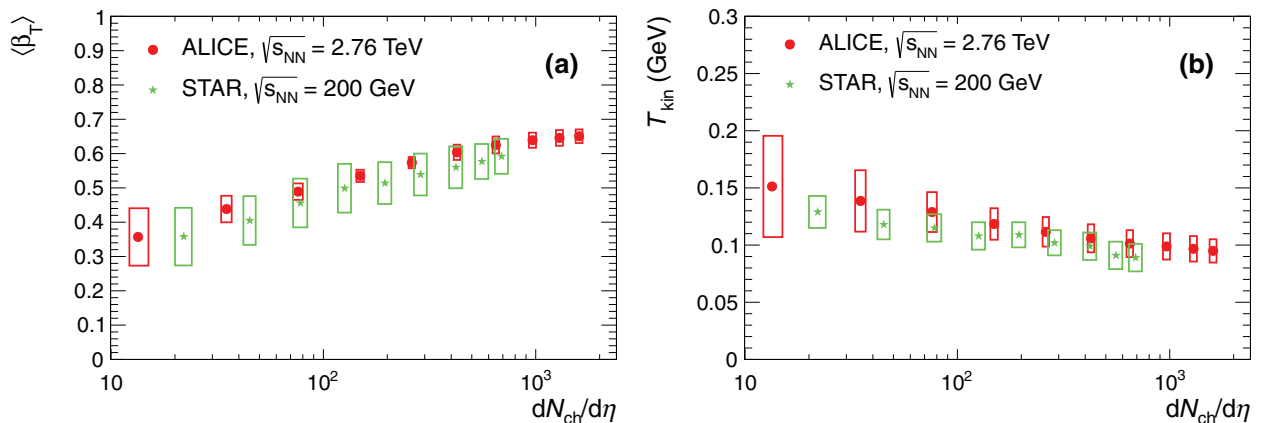
FIG. 11. (Color online) Blast-wave parameters (a) $\langle \beta_T \rangle$ and (b) T_{kin} as a function of $dN_{ch}/d\eta$ compared to previous results at $\sqrt{s_{NN}} = 200$ GeV [5] (full systematic uncertainties for both experiments).
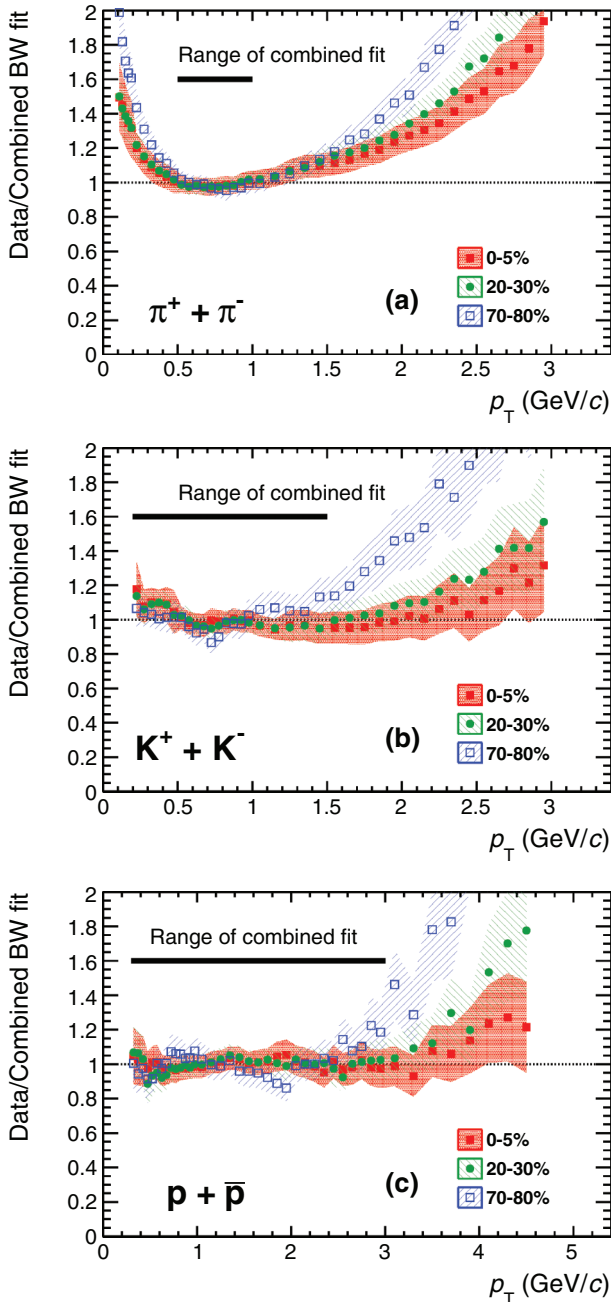
FIG. 12. (Color online) Ratio of the measured spectra to the combined blast-wave fit as a function of p_T for (a) π, (b) K, and (c) p.

In order to further test the stability of the fit, it was repeated in the ranges 0.7–1.3 GeV/c, 0.5–1.5 GeV/c, 1–3 GeV/c ("high p_T") and 0.5–0.8 GeV/c, 0.2–1 GeV/c, and 0.3–1.5 GeV/c ("low p_T") for π, K, p, respectively. The effect of the fit ranges is demonstrated in Fig. 10(b). As can be seen, while the value of $\langle \beta_T \rangle$ is relatively stable, especially for the most central bins, the value of $T_{\rm kin}$ is strongly affected by the fit range, with differences of order 15 MeV for the most central events. For most peripheral events, $\langle \beta_T \rangle$ shows some instability. However, it should be noticed that this parameter is mostly fixed by the low-p_T protons and its uncertainty
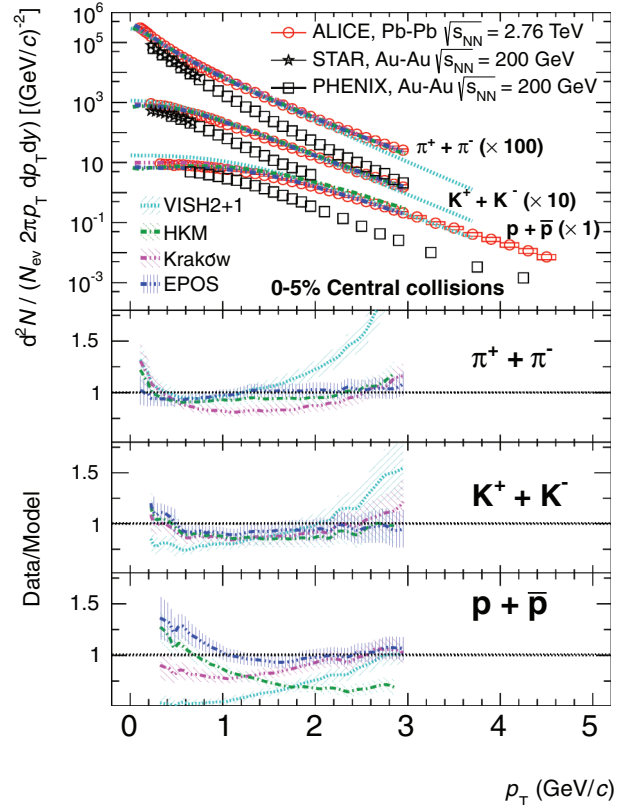
FIG. 13. (Color online) Spectra of particles for summed charge states in the centrality bin 0–5% compared to hydrodynamical models and results from RHIC at $\sqrt{s_{NN}}$ = 200 GeV [42,45]. See text for details. Systematic uncertainties plotted (boxes); statistical uncertainties are smaller than the symbol size.

increases significantly when the fit range for the protons is reduced.

The combined fits in the default range are shown in Fig. 4, compared to fits to individual particle spectra. The dotted curves represent the combined blast-wave fits, while the dashed curves are the individual fits to each species. The individual fits reproduce the spectra over the full p_T range in all centrality bins, thus allowing for a reliable estimate of the $\langle p_T \rangle$ and integrated yields, as mentioned above. The extrapolation at low and high p_T of the combined fits gets progressively worse for decreasing centrality. The ratios of the spectra to the combined fits are shown in Fig. 12. If the behavior of the spectra is purely hydrodynamical over the full p_T range considered, one would expect that the fireball blast-wave parameters determined by a fit in a limited p_T range are able to predict the full shape. This is what is observed in the most central bin for protons and kaons. The same is not true for the more peripheral bins, and the p_T threshold at which the function deviates from the data decreases with centrality, indicating the limit of applicability of the hydrodynamical picture (as also discussed below).

The spectra for summed charge states in central (0–5%), semicentral (20–30%), and peripheral (70–80%) collisions are compared to hydrodynamical models and previous results in Au-Au collisions at $\sqrt{s_{NN}}$ = 200 GeV in Figs. 13, 14, and 15.
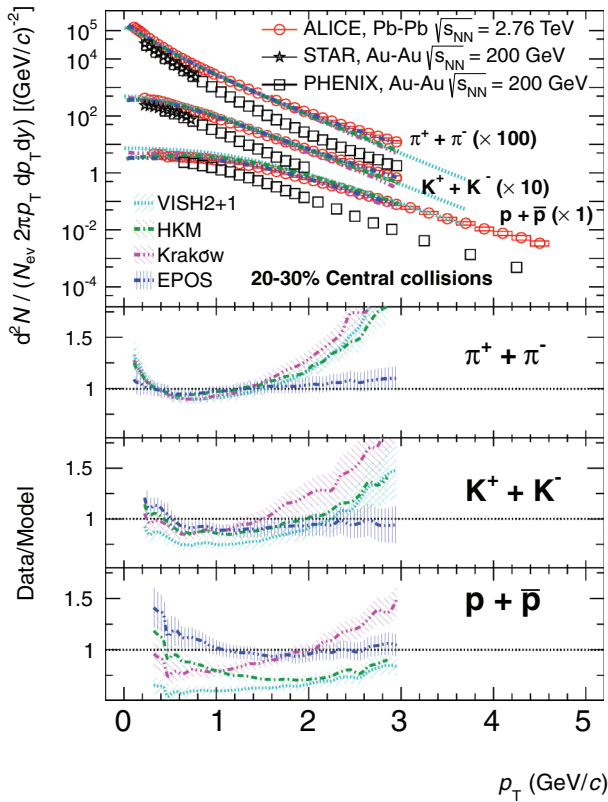
FIG. 14. (Color online) Spectra of particles for summed charge states in the centrality bin 20–30% compared to hydrodynamical models and results from RHIC at $\sqrt{s_{NN}} = 200$ GeV [42,45]. See text for details. Systematic uncertainties plotted (boxes); statistical uncertainties are smaller than the symbol size.

FIG. 15. (Color online) Spectra of particles for summed charge states in the centrality bin 70–80% compared to hydrodynamical models and results from RHIC at $\sqrt{s_{NN}} = 200$ GeV [42,45]. See text for details. Systematic uncertainties plotted (boxes); statistical uncertainties are smaller than the symbol size.

A dramatic change in spectral shapes from RHIC to LHC energies is observed, with the protons in particular showing a flatter distribution. A comparison between the two energies based on the values of $\langle \beta_T \rangle$ and T_{kin} from the combined blast-wave fits [5] is shown in Figs. 10 and 11. For central collisions, about 10% stronger radial flow than at RHIC is observed at the LHC.[2]

The models shown in Figs. 13, 14, and 15 give for central collisions a fair description of the data. In the region $p_T \lesssim 3$ GeV/c (Kraków [46]), $p_T \lesssim 1.5$ GeV/c (HKM [47]), and $p_T \lesssim 3$ GeV/c (EPOS [48], with the exception of protons which are underestimated by about 30% at low p_T), the models describe the experimental data within $\sim 20\%$, supporting a hydrodynamic interpretation of the p_T spectra in central collisions at the LHC. VISH2 + 1 [49] is a viscous hydrodynamic model that reproduces fairly well the pion and kaon distributions up to $p_T \sim 2$ GeV/c, but it misses the protons, both in shape and absolute abundance in all centrality

bins. In this version of the model the yields are thermal, with a chemical temperature $T_{\mathrm{ch}} = 165$ MeV, extrapolated from lower energies. The difference between VISH2 + 1 and the data are possibly due to the lack of an explicit description of the hadronic phase in the model. This idea is supported by the comparison with HKM [47,50]. HKM is an ideal hydrodynamics model, in which after the hydrodynamic phase particles are injected into a hadronic cascade model (UrQMD), which further transports them until final decoupling. The hadronic phase builds up additional radial flow and affects particle ratios due to the hadronic interactions. As can be seen, this model yields a better description of the data. The protons at low p_T, and, hence, their total number, are rather well reproduced, even if the slope is significantly smaller than in the data. Antibaryon-baryon annihilation is an important ingredient for the description of particle yields in this model [47,50]. The Kraków [51,52] model, on the other hand, uses an ansatz to describe deviation from equilibrium due to bulk viscosity corrections at freeze-out, which seems successful in reproducing the data. A general feature of these models is that, going to more peripheral events, the theoretical curves deviate from the data at high p_T (Figs. 14 and 15). This is similar to what is observed in the comparison to the blast-wave fits and shows the limits of the hydrodynamical models. As speculated in Ref. [46], this could indicate the onset of a nonthermal (hard) component, which in more peripheral collisions is

---

[2]The full systematic uncertainties on the parameters, quoted by both STAR and ALICE, include a number of checks on the stability of the fit which have a similar effect at different energies. When comparing results of different experiments, only the statistical and systematic uncertainties of the p_T distributions should be considered, but not those related to the stability of the fit.

not dominated by the flow-boosted thermal component. This picture is further substantiated by the change in the local slopes as seen in Fig. 6.

The EPOS (2.17v3) model [48] aims at describing all p_T domains with the same dynamical picture. In this model, the initial hard scattering creates "flux tubes" which either escape the medium and hadronize as jets or contribute to the bulk matter, described in terms of hydrodynamics. After hadronization, particles are transported with a hadronic cascade model (UrQMD). EPOS shows a good agreement with the data for central and semicentral collisions. A calculation done with the same model, but disabling the late hadronic phase, yields a significantly worse description [48], indicating the important role of the late hadronic interactions in this model. An EPOS calculation for peripheral collisions was not available at the time of writing, but it will be important to see how well the peripheral data can be described in this model, since it should include all relevant physics processes. Several other models implementing similar ideas (hydrodynamics model coupled to a hadronic cascade code, possibly with a description of fluctuations in the initial condition) are available in the literature [53,54] but not discussed in this paper. The simultaneous description of additional variables, such as the v_n azimuthal flow coefficients within the same model, will help in differentiating different hydrodynamical model scenarios.

Figure 16 shows the $p/\pi = (p + \bar{p})/(\pi^+ + \pi^-)$ and $K/\pi = (K^+ + K^-)/(\pi^+ + \pi^-)$ ratios as a function of p_T. Both ratios are seen to increase as a function of centrality at intermediate p_T with a corresponding depletion at low p_T (the p_T integrated ratios show little dependence on centrality, Fig. 9). The p/π ratio, in particular, shows a more pronounced increase, reaching a value of about 0.9 at $p_T = 3$ GeV/c. This is reminiscent of the increase in the baryon-to-meson ratio observed at RHIC in the intermediate p_T region [19,57], which is suggestive of the recombination picture discussed in Sec. I. It should be noted, however, that a rise of the ratio with p_T is an intrinsic feature of hydrodynamical models, where it is just due to the mass ordering induced by radial flow (heavier particles are pushed to higher p_T by the collective motion). In Fig. 16 a prediction from two of the hydrodynamical models discussed above [47,52] and a prediction from a recombination model [20,55,56] are shown. As can be seen, the ratio for central events is reasonably reproduced by the Kraków hydrodynamical model, while HKM only reproduces the data up to $p_T \sim$ 1.5 GeV/c and the recombination prediction is higher than the data and predicts a flatter trend in the range 2–3 GeV/c.

This measurement is currently being extended to higher p_T by ALICE using the HMPID detector (High Momentum Particle Identification [58], a ring-imaging Čerenkov), complemented by a statistical identification in the relativistic rise region of the TPC. A complementary study of the Λ/K_S^0 ratio will also provide a good p_T coverage and additional constraints.

B. p_T-integrated yields

The integrated ratios can be interpreted in terms of the thermal models. Figure 9 depicts the expectations from these
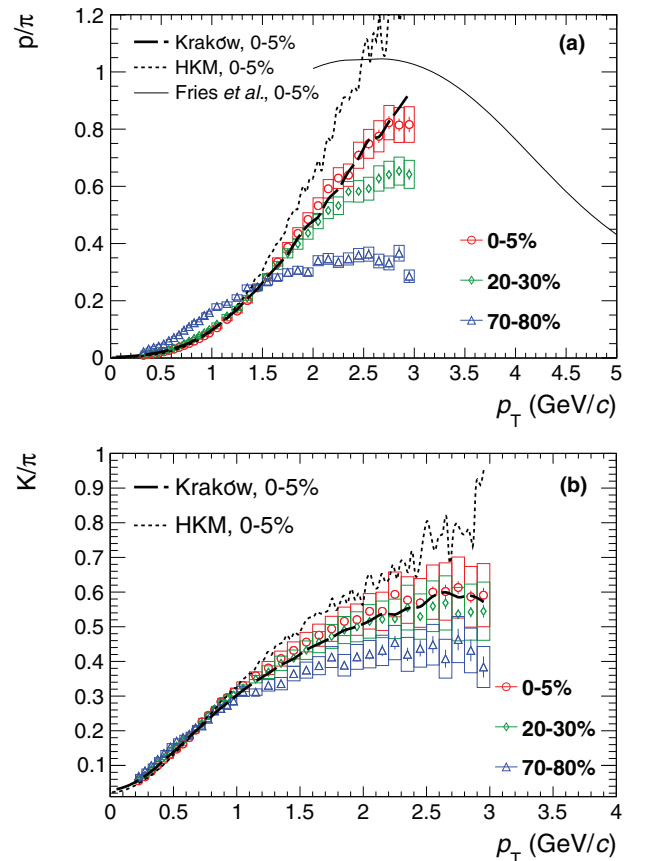
FIG. 16. (Color online) (a) $p/\pi = (p + \bar{p})/(\pi^+ + \pi^-)$ as a function of p_T for different centrality bins compared to ratios from the Kraków [46] and HKM [47] hydrodynamic models and to a recombination model [20,55,56]; (b) $K/\pi = (K^+ + K^-)/(\pi^+ + \pi^-)$ ratio as a function of p_T for different centrality bins compared to ratios from the Kraków [46] and HKM [47] hydrodynamic models.

models, which, based on lower-energy data, used the values $T \simeq 160$–170 MeV and $\mu_B \simeq 1$ MeV at the LHC [59,60]. The K/π ratio is consistent with these expectations, while the p/π ratio is found to be lower by a factor of about 1.5. As discussed in Ref. [18], this finding was one of the surprises of the first Pb-Pb run at the LHC and still needs to be understood.

Some indication of a similar disagreement between data and the thermal model is also seen in the RHIC data, with the proton measurements being 10–20% lower than the thermal model predictions [5,11]. This discrepancy was not considered to be significant due to experimental uncertainties in the subtraction of secondary particles, differences between thermal model implementations, and model uncertainties [61].

C. Total proton spectrum

In order to compare directly with lower-energy results, we performed a measurement of protons including feed-down from weak decays ("total proton spectrum"), based on tracks reconstructed using only TPC information, with no requirements on the ITS. These tracks have a similar efficiency for both primary and secondary particles, with the
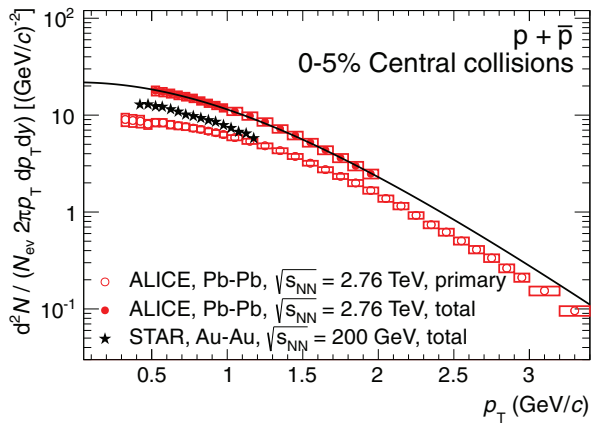
FIG. 17. (Color online) Transverse-momentum p_T distribution of total protons based on tracks reconstructed using only TPC information (full circles) compared to primary protons (open circles) and corresponding total spectra measured by the STAR collaboration in Au-Au collisions at $\sqrt{s_{NN}} = 200$ GeV/c (full stars). 0–5% most central events. Box: systematic uncertainty. Statistical uncertainties smaller than the symbols. Curve: individual blast-wave fit.

difference in the particle composition between data and Monte Carlo being of minor importance. The reconstructed sample thus already includes most of the secondary particles. The efficiency correction for the total proton measurement is about 25% at 450 MeV/c and 5% at 1 GeV/c. In this analysis, the secondaries from detector material were subtracted using a DCA$_{xy}$ fit procedure, similar to the one discussed in Sec. II. The total proton spectrum for central collisions (0–5%) is compared in Fig. 17 with the primary proton spectrum and with the previous STAR measurements of total protons at $\sqrt{s_{NN}} = 200$ GeV. The comparison of the spectra confirms the change in shape and yield from RHIC to LHC, already discussed for primary protons. The total spectrum was fitted with a blast-wave function (also shown in Fig. 17) to compute the extrapolation for the extraction of the integrated yield. Due to the limited p_T coverage of the TPC-only analysis, the fraction of the extrapolated yield amounts to about 25%, resulting in a larger extrapolation uncertainty (about 12%) as compared to the primary spectrum. We found $dN^{\text{total}}_{p+\bar{p}}/dy = 120 \pm 20(\text{syst.} + \text{stat.})$ for the combined spectra of protons and antiprotons, resulting in the ratio p (total)$/\pi = 0.082 \pm 0.010$. This is about 15% lower than the ratio of 0.095 ± 0.011 [42] measured by STAR at $\sqrt{s_{NN}} = 200$ GeV (consistent with what was previously noted for primary protons), but the difference is not significant within uncertainties.

Subtraction of the total and primary proton yields $dN^{\text{sec}}_{p+\bar{p}}/dy = 53 \pm 19(\text{syst.} + \text{stat.})$ for secondary protons. This number, normalized to the primary pion yield, can be compared to the thermal model prediction [12] with $T_{\text{ch}} = 164$ MeV. There are five main contributions to the secondary protons, summarized in Table VI. Rescaling the ratios shown in Table VI by the measured pion yield, we get $dN^{\text{sec,model}}_{p+\bar{p}}/dy = 62$, in good agreement with the measurement. This result suggests that the disagreement between the data and the thermal model is most prominent for primary protons, while strange baryons contributing to the production of secondary protons

TABLE VI. Contribution to secondary protons estimated in the thermal model [12] with $T_{\text{ch}} = 164$ MeV.

Particle	Decay channel	Branching ratio	p (secondary)$/\pi$
Λ	$p\pi$	63.9%	4.42×10^{-2}
Σ^+	$p\pi^0$	51.6%	1.27×10^{-2}
Ξ^-	$\Lambda\pi$	99.89%	5.49×10^{-3}
Ξ^0	$\Lambda\pi$	99.53%	5.58×10^{-3}
Ω	ΛK	67.8%	9.83×10^{-4}

are likely better described. If the total protons measured in the data and in the thermal model are compared, the disagreement gets partially suppressed, because the number of secondaries is well reproduced in the thermal model and the fraction of secondary protons is rather large ($\sim$50%).

A possible explanation for the difference between the p/π ratio and the predictions from the thermal models is antibaryon-baryon annihilation in the hadronic phase [47,62, 63]. The p/π ratio depicted in Fig. 9 suggests a decreasing trend with centrality, consistent with the antibaryon-baryon annihilation hypothesis: The effect is expected to be less important for the more dilute system created in peripheral collisions. It should be noted that all the available models incorporating a hadronic phase use the UrQMD [64,65] hadronic cascade model, and the effects induced by the hadronic phase are model dependent. While this microscopic model includes annihilation processes, it does not implement the reverse process like $n\pi \rightarrow p\bar{p}$. The effect of the reverse reactions was investigated in a recent calculation [66]. It was found to be non-negligible, while the net suppression of baryons is still very significant.

The origin of the low proton yield with respect to the thermal model expectations is not yet established and alternative explanations exist in the literature. Implementations of the thermal model incorporating nonequilibrium effects predict a reduction of the p/π ratio, although the details depend on the exact value of model parameters. With the preferred set of parameters in Ref. [67], the authors could predict the correct value for p/π but not for K/π. This is explained in Ref. [68] as a lower strangeness-over-entropy ratio as compared to the expectations. An alternative explanation may come from the existence of flavor- and mass-dependent prehadronic bound states in the QGP phase, as suggested by recent lattice QCD calculation and QCD-inspired models [69,70]. Additional constraints to discriminate between these different scenarios will be provided by a thermal analysis, including, in particular, strange and multistrange baryons.

VI. CONCLUSIONS

In this paper we presented a comprehensive measurement of π, K, and p production in Pb-Pb collisions at $\sqrt{s_{NN}} = 2.76$ TeV at the LHC. Antiparticle-to-particle ratios are compatible with unity at all p_T and at all centralities, as expected for LHC. A clear evolution of all spectra with centrality is seen, with an almost exponential behavior at high p_T and a flattening of the spectra at low p_T. These features

are compatible with the development of a strong collective flow with centrality, which dominates the spectral shapes up to relatively high p_T in central collisions. The $\langle \beta_T \rangle$ parameter extracted from fits to the blast-wave parametrization indicates a radial flow about 10% higher than at RHIC at $\sqrt{s_{NN}} = 200$ GeV in central collisions. The integrated abundances of particles are almost independent of centrality. They are compared with expectations from thermal models. While the K/π ratio was found to agree with these expectations, the p/π is a factor 1.5 lower. The central collision data are successfully described by hydrodynamic models, but the low proton yield requires a refined description of the late fireball stages. These models [47,48] indicate a non-negligible baryon annihilation in the hadronic phase, which alters the thermal yields and leads to a lower proton yield. The origin of this effect, however, is not yet established and alternative explanations, such as nonequilibrium effects or flavor-dependent freeze-out, exist in the literature. In more peripheral collisions, purely hydrodynamic models give a poor description of the data, indicating the limit of applicability of hydrodynamics.

[1] U. W. Heinz and M. Jacob, arXiv:nucl-th/0002042.

[2] I. Arsene *et al.* (BRAHMS Collaboration), Nucl. Phys. A **757**, 1 (2005).

[3] K. Adcox *et al.* (PHENIX Collaboration), Nucl. Phys. A **757**, 184 (2005).

[4] B. Back, M. Baker, M. Ballintijn, D. Barton, B. Becker *et al.* Nucl. Phys. A **757**, 28 (2005).

[5] J. Adams *et al.* (STAR Collaboration), Nucl. Phys. A **757**, 102 (2005).

[6] E. V. Shuryak, Nucl. Phys. A **750**, 64 (2005).

[7] P. Huovinen and P. Ruuskanen, Annu. Rev. Nucl. Part. Sci. **56**, 163 (2006).

[8] B. Müller and J. L. Nagle, Annu. Rev. Nucl. Part. Sci. **56**, 93 (2006).

[9] E. Schnedermann, J. Sollfrank, and U. W. Heinz, Phys. Rev. C **48**, 2462 (1993).

[10] U. W. Heinz, arXiv:hep-ph/0407360.

[11] A. Andronic, P. Braun-Munzinger, K. Redlich, and J. Stachel, J. Phys. G **38**, 124081 (2011).

[12] A. Andronic, P. Braun-Munzinger, and J. Stachel, Phys. Lett. B **673**, 142 (2009).

[13] F. Becattini and R. Fries, *Landolt-Boernstein, Relativistic Heavy Ion Physics* (Springer, Berlin, 2010).

[14] J. Cleymans and K. Redlich, Phys. Rev. Lett. **81**, 5284 (1998).

[15] R. Rapp and E. V. Shuryak, Phys. Rev. Lett. **86**, 2980 (2001).

[16] P. Braun-Munzinger, J. Stachel, and C. Wetterich, Phys. Lett. B **596**, 61 (2004).

[17] U. Heinz and G. Kestin, PoS **CPOD2006**, 038 (2006).

[18] B. Abelev *et al.* (ALICE Collaboration), Phys. Rev. Lett. **109**, 252301 (2012).

[19] B. Abelev *et al.* (STAR Collaboration), Phys. Rev. Lett. **97**, 152301 (2006).

[20] R. Fries, B. Muller, C. Nonaka, and S. Bass, Phys. Rev. Lett. **90**, 202303 (2003).

[21] V. Greco, C. Ko, and P. Levai, Phys. Rev. Lett. **90**, 202302 (2003).

[22] K. Aamodt *et al.* (ALICE Collaboration), Eur. Phys. J. C **71**, 1 (2011).

[23] B. Alessandro *et al.* (ALICE Collaboration), J. Phys. G **32**, 1295 (2006).

[24] K. Aamodt *et al.* (ALICE Collaboration), J. Instrum. **3**, S08002 (2008).

[25] B. Abelev *et al.* (ALICE Collaboration), Phys. Rev. C **88**, 044909 (2013).

[26] K. Aamodt *et al.* (ALICE Collaboration), Phys. Rev. Lett. **106**, 032301 (2011).

[27] K. Aamodt *et al.* (ALICE Collaboration), Phys. Rev. Lett. **105**, 252301 (2010).

[28] B. Abelev *et al.* (ALICE Collaboration), Phys. Rev. Lett. **109**, 252302 (2012).

[29] K. Aamodt *et al.* (ALICE Collaboration), Eur. Phys. J. C **68**, 89 (2010).

[30] J. Beringer *et al.* (Particle Data Group), Phys. Rev. D **86**, 010001 (2012), Chap. 30.

[31] X.-N. Wang and M. Gyulassy, Phys. Rev. D **44**, 3501 (1991).

[32] R. Brun, F. Carminati, and S. Giani, CERN-W5013 (1994).

[33] S. Agostinelli *et al.* (GEANT4), Nucl. Instrum. Methods A **506**, 250 (2003).

[34] G. Battistoni, S. Muraro, P. R. Sala, F. Cerutti, A. Ferrari *et al.*, AIP Conf. Proc. **896**, 31 (2007).

[35] K. Aamodt *et al.* (ALICE Collaboration), Phys. Rev. Lett. **105**, 072002 (2010).

[36] T. Lee and R. Redwine, Annu. Rev. Nucl. Part. Sci. **52**, 23 (2002).

[37] E. Friedman, A. Gal, R. Weiss, J. Aclander, J. Alster *et al.*, Phys. Rev. C **55**, 1304 (1997).

[38] D. Ashery, I. Navon, G. Azuelos, H. Walter, H. Pfeiffer *et al.*, Phys. Rev. C **23**, 2173 (1981).

[39] R. Carlson, At. Data Nucl. Data Tables **63**, 93 (1996).

[40] G. Bendiscioli and D. Kharzeev, Riv. Nuovo Cimento **17N6**, 1 (1994).

[41] J. Sollfrank, P. Koch, and U. W. Heinz, Phys. Lett. B **252**, 256 (1990).

[42] B. Abelev *et al.* (STAR Collaboration), Phys. Rev. C **79**, 034909 (2009).

[43] S. Adler *et al.* (PHENIX Collaboration), Phys. Rev. C **71**, 034908 (2005).

[44] I. Bearden *et al.* (BRAHMS Collaboration), Phys. Rev. Lett. **88**, 202301 (2002).

[45] S. S. Adler *et al.* (PHENIX Collaboration), Phys. Rev. C **69**, 034909 (2004).

[46] P. Bozek and I. Wyskiel-Piekarska, arXiv:1203.6513.

[47] I. Karpenko, Y. Sinyukov, and K. Werner, Phys. Rev. C **87**, 024914 (2013).

[48] K. Werner, I. Karpenko, M. Bleicher, T. Pierog, and S. Porteboeuf-Houssais, Phys. Rev. C **85**, 064907 (2012).

[49] C. Shen, U. Heinz, P. Huovinen, and H. Song, Phys. Rev. C **84**, 044903 (2011).

[50] Y. Karpenko and Y. Sinyukov, J. Phys. G **38**, 124059 (2011).

[51] P. Bozek, Phys. Rev. C **85**, 034901 (2012).

[52] P. Bozek, Acta Phys. Polon. B **43**, 689 (2012).

[53] S. Ryu, S. Jeon, C. Gale, B. Schenke, and C. Young, Nucl. Phys. A **904–905**, 389c (2013).

[54] H. Petersen, Phys. Rev. C **84**, 034912 (2011).

[55] R. Fries, B. Muller, C. Nonaka, and S. Bass, Phys. Rev. C **68**, 044902 (2003).

[56] R. Fries (private communication) (2012).

[57] M. Lamont, Eur. Phys. J. C **49**, 35 (2007).

[58] ALICE TDR 1, Technical Report No. LHCC 9819, 1998.

[59] J. Cleymans, I. Kraus, H. Oeschler, K. Redlich, and S. Wheaton, Phys. Rev. C **74**, 034903 (2006).

[60] A. Andronic, P. Braun-Munzinger, and J. Stachel, Nucl. Phys. A **772**, 167 (2006).

[61] F. Becattini, P. Castorina, A. Milov, and H. Satz, Eur. Phys. J. C **66**, 377 (2010).

[62] F. Becattini, M. Bleicher, T. Kollegger, T. Schuster, J. Steinheimer, and R. Stock, Phys. Rev. Lett. **111**, 082302 (2013).

[63] J. Steinheimer, J. Aichelin, and M. Bleicher, Phys. Rev. Lett. **110**, 042501 (2013).

[64] M. Bleicher, E. Zabrodin, C. Spieles, S. Bass, C. Ernst *et al.*, J. Phys. G **25**, 1859 (1999).

[65] S. Bass, M. Belkacem, M. Bleicher, M. Brandstetter, L. Bravina *et al.*, Prog. Part. Nucl. Phys. **41**, 255 (1998).

[66] Y. Pan and S. Pratt, arXiv:1210.1577.

[67] J. Rafelski and J. Letessier, Phys. Rev. C **83**, 054909 (2011).

[68] M. Petran, J. Letessier, V. Petracek, and J. Rafelski, arXiv:1303.2098.

[69] C. Ratti, R. Bellwied, M. Cristoforetti, and M. Barbaro, Phys. Rev. D **85**, 014004 (2012).

[70] R. Bellwied, PoS **BORMIO2012**, 045 (2012).

B. Abelev,[1] J. Adam,[2] D. Adamová,[3] A. M. Adare,[4] M. M. Aggarwal,[5] G. Aglieri Rinella,[6] A. Agnello,[7,8] A. G. Agocs,[9] A. Agostinelli,[10] Z. Ahammed,[11] N. Ahmad,[12] A. Ahmad Masoodi,[12] S. A. Ahn,[13] S. U. Ahn,[13] M. Ajaz,[14] A. Akindinov,[15] D. Aleksandrov,[16] B. Alessandro,[7] A. Alici,[17,18] A. Alkin,[19] E. Almaráz Aviña,[20] J. Alme,[21] T. Alt,[22] V. Altini,[23] S. Altinpinar,[24] I. Altsybeev,[25] C. Andrei,[26] A. Andronic,[27] V. Anguelov,[28] J. Anielski,[29] C. Anson,[30] T. Antičić,[31] F. Antinori,[32] P. Antonioli,[17] L. Aphecetche,[33] H. Appelshäuser,[34] N. Arbor,[35] S. Arcelli,[10] A. Arend,[34] N. Armesto,[36] R. Arnaldi,[7] T. Aronsson,[4] I. C. Arsene,[27] M. Arslandok,[34] A. Asryan,[25] A. Augustinus,[6] R. Averbeck,[27] T. C. Awes,[37] J. Äystö,[38] M. D. Azmi,[12,39] M. Bach,[22] A. Badalà,[40] Y. W. Baek,[41,42] R. Bailhache,[34] R. Bala,[43,7] A. Baldisseri,[44] F. Baltasar Dos Santos Pedrosa,[6] J. Bán,[45] R. C. Baral,[46] R. Barbera,[47] F. Barile,[23] G. G. Barnaföldi,[9] L. S. Barnby,[48] V. Barret,[41] J. Bartke,[49] M. Basile,[10] N. Bastid,[41] S. Basu,[11] B. Bathen,[29] G. Batigne,[33] B. Batyunya,[50] C. Baumann,[34] I. G. Bearden,[51] H. Beck,[34] N. K. Behera,[52] I. Belikov,[53] F. Bellini,[10] R. Bellwied,[54] E. Belmont-Moreno,[20] G. Bencedi,[9] S. Beole,[55] I. Berceanu,[26] A. Bercuci,[26] Y. Berdnikov,[56]

D. Berenyi,[9] A. A. E. Bergognon,[33] D. Berzano,[55,7] L. Betev,[6] A. Bhasin,[43] A. K. Bhati,[5] J. Bhom,[57] L. Bianchi,[55] N. Bianchi,[58] J. Bielčík,[2] J. Bielčíková,[3] A. Bilandzic,[51] S. Bjelogrlic,[59] F. Blanco,[54] F. Blanco,[60] D. Blau,[16] C. Blume,[34] M. Boccioli,[6] S. Böttger,[61] A. Bogdanov,[62] H. Bøggild,[51] M. Bogolyubsky,[63] L. Boldizsár,[9] M. Bombara,[64] J. Book,[34] H. Borel,[44] A. Borissov,[65] F. Bossú,[39] M. Botje,[66] E. Botta,[55] E. Braidot,[67] P. Braun-Munzinger,[27] M. Bregant,[33] T. Breitner,[61] T. A. Broker,[34] T. A. Browning,[68] M. Broz,[69] R. Brun,[6] E. Bruna,[55,7] G. E. Bruno,[23] D. Budnikov,[70] H. Buesching,[34] S. Bufalino,[55,7] P. Buncic,[6] O. Busch,[28] Z. Buthelezi,[39] D. Caffarri,[71,32] X. Cai,[72] H. Caines,[4] E. Calvo Villar,[73] P. Camerini,[74] V. Canoa Roman,[75] G. Cara Romeo,[17] F. Carena,[6] W. Carena,[6] N. Carlin Filho,[76] F. Carminati,[6] A. Casanova Díaz,[58] J. Castillo Castellanos,[44] J. F. Castillo Hernandez,[27] E. A. R. Casula,[77] V. Catanescu,[26] C. Cavicchioli,[6] C. Ceballos Sanchez,[78] J. Cepila,[2] P. Cerello,[7] B. Chang,[38,79] S. Chapeland,[6] J. L. Charvet,[44] S. Chattopadhyay,[80] S. Chattopadhyay,[11] M. Cherney,[81] C. Cheshkov,[6,82] B. Cheynis,[82] V. Chibante Barroso,[6] D. D. Chinellato,[54] P. Chochula,[6] M. Chojnacki,[51] S. Choudhury,[11] P. Christakoglou,[66] C. H. Christensen,[51] P. Christiansen,[83] T. Chujo,[57] S. U. Chung,[84] C. Cicalo,[85] L. Cifarelli,[10,6,18] F. Cindolo,[17] J. Cleymans,[39] F. Colamaria,[23] D. Colella,[23] A. Collu,[77] G. Conesa Balbastre,[35] Z. Conesa del Valle,[6] M. E. Connors,[4] G. Contin,[74] J. G. Contreras,[75] T. M. Cormier,[65] Y. Corrales Morales,[55] P. Cortese,[86] I. Cortés Maldonado,[87] M. R. Cosentino,[67] F. Costa,[6] M. E. Cotallo,[60] E. Crescio,[75] P. Crochet,[41] E. Cruz Alaniz,[20] R. Cruz Albino,[75] E. Cuautle,[88] L. Cunqueiro,[58] A. Dainese,[71,32] A. Danu,[89] K. Das,[80] I. Das,[90] S. Das,[91] D. Das,[80] S. Dash,[52] A. Dash,[92] S. De,[11] G. O. V. de Barros,[76] A. De Caro,[93,18] G. de Cataldo,[94] J. de Cuveland,[22] A. De Falco,[77] D. De Gruttola,[18] H. Delagrange,[33] A. Deloff,[95] N. De Marco,[7] E. Dénes,[9] S. De Pasquale,[93] A. Deppman,[76] G. D. Erasmo,[23] R. de Rooij,[59] M. A. Diaz Corchero,[60] D. Di Bari,[23] T. Dietel,[29] C. Di Giglio,[23] S. Di Liberto,[96] A. Di Mauro,[6] P. Di Nezza,[58] R. Divià,[6] Ø. Djuvsland,[24] A. Dobrin,[65,83] T. Dobrowolski,[95] B. Dönigus,[27] O. Dordic,[97] O. Driga,[33] A. K. Dubey,[11] A. Dubla,[59] L. Ducroux,[82] P. Dupieux,[41] A. K. Dutta Majumdar,[80] D. Elia,[94] D. Emschermann,[29] H. Engel,[61] B. Erazmus,[6,33] H. A. Erdal,[21] B. Espagnon,[90] M. Estienne,[33] S. Esumi,[57] D. Evans,[48] G. Eyyubova,[97] D. Fabris,[71,32] J. Faivre,[35] D. Falchieri,[10] A. Fantoni,[58] M. Fasel,[27,28] R. Fearick,[39] D. Fehlker,[24] L. Feldkamp,[29] D. Felea,[89] A. Feliciello,[7] B. Fenton-Olsen,[67] G. Feofilov,[25] A. Fernández Téllez,[87] A. Ferretti,[55] A. Festanti,[71] J. Figiel,[49] M. A. S. Figueredo,[76] S. Filchagin,[70] D. Finogeev,[98] F. M. Fionda,[23] E. M. Fiore,[23] E. Floratos,[99] M. Floris,[6] S. Foertsch,[39] P. Foka,[27] S. Fokin,[16] E. Fragiacomo,[100] A. Francescon,[6,71] U. Frankenfeld,[27] U. Fuchs,[6] C. Furget,[35] M. Fusco Girard,[93] J. J. Gaardhøje,[51] M. Gagliardi,[55] A. Gago,[73] M. Gallio,[55] D. R. Gangadharan,[30] P. Ganoti,[37] C. Garabatos,[27] E. Garcia-Solis,[101] C. Gargiulo,[6] I. Garishvili,[1] J. Gerhard,[22] M. Germain,[33] C. Geuna,[44] A. Gheata,[6] M. Gheata,[89,6] B. Ghidini,[23] P. Ghosh,[11] P. Gianotti,[58] M. R. Girard,[102] P. Giubellino,[6] E. Gladysz-Dziadus,[49] P. Glässel,[28] R. Gomez,[103,75] E. G. Ferreiro,[36] L. H. González-Trueba,[20] P. González-Zamora,[60] S. Gorbunov,[22] A. Goswami,[104] S. Gotovac,[105] L. K. Graczykowski,[102] R. Grajcarek,[28] A. Grelli,[59] A. Grigoras,[6] C. Grigoras,[6] V. Grigoriev,[62] S. Grigoryan,[50] A. Grigoryan,[106] B. Grinyov,[19] N. Grion,[100] P. Gros,[83] J. F. Grosse-Oetringhaus,[6] J.-Y. Grossiord,[82] R. Grosso,[6] F. Guber,[98] R. Guernane,[35] B. Guerzoni,[10] M. Guilbaud,[82] K. Gulbrandsen,[51] H. Gulkanyan,[106] T. Gunji,[107] R. Gupta,[43] A. Gupta,[43] R. Haake,[29] Ø. Haaland,[24] C. Hadjidakis,[90] M. Haiduc,[89] H. Hamagaki,[107] G. Hamar,[9] B. H. Han,[108] L. D. Hanratty,[48] A. Hansen,[51] Z. Harmanová-Tóthová,[64] J. W. Harris,[4] M. Hartig,[34] A. Harton,[101] D. Hatzifotiadou,[17] S. Hayashi,[107] A. Hayrapetyan,[6,106] S. T. Heckel,[34] M. Heide,[29] H. Helstrup,[21] A. Herghelegiu,[26] G. Herrera Corral,[75] N. Herrmann,[28] B. A. Hess,[109] K. F. Hetland,[21] B. Hicks,[4] B. Hippolyte,[53] Y. Hori,[107] P. Hristov,[6] I. Hřivnáčová,[90] M. Huang,[24] T. J. Humanic,[30] D. S. Hwang,[108] R. Ichou,[41] R. Ilkaev,[70] I. Ilkiv,[95] M. Inaba,[57] E. Incani,[77] G. M. Innocenti,[55] P. G. Innocenti,[6] M. Ippolitov,[16] M. Irfan,[12] C. Ivan,[27] M. Ivanov,[27] A. Ivanov,[25] V. Ivanov,[56] O. Ivanytskyi,[19] A. Jachołkowski,[47] P. M. Jacobs,[67] H. J. Jang,[13] M. A. Janik,[102] R. Janik,[69] P. H. S. Y. Jayarathna,[54] S. Jena,[52] D. M. Jha,[65] R. T. Jimenez Bustamante,[88] P. G. Jones,[48] H. Jung,[42] A. Jusko,[48] A. B. Kaidalov,[15] S. Kalcher,[22] P. Kaliňák,[45] T. Kalliokoski,[38] A. Kalweit,[110,6] J. H. Kang,[79] V. Kaplin,[62] A. Karasu Uysal,[6,111,112] O. Karavichev,[98] T. Karavicheva,[98] E. Karpechev,[98] A. Kazantsev,[16] U. Kebschull,[61] R. Keidel,[113] M. M. Khan,[12] K. H. Khan,[14] P. Khan,[80] S. A. Khan,[11] A. Khanzadeev,[56] Y. Kharlov,[63] B. Kileng,[21] T. Kim,[79] J. S. Kim,[42] D. J. Kim,[38] S. Kim,[108] M. Kim,[79] B. Kim,[79] M. Kim,[42] D. W. Kim,[42,13] J. H. Kim,[108] S. Kirsch,[22] I. Kisel,[22] S. Kiselev,[15] A. Kisiel,[102] J. L. Klay,[114] J. Klein,[28] C. Klein-Bösing,[29] M. Kliemant,[34] A. Kluge,[6] M. L. Knichel,[27] A. G. Knospe,[115] M. K. Köhler,[27] T. Kollegger,[22] A. Kolojvari,[25] M. Kompaniets,[25] V. Kondratiev,[25] N. Kondratyeva,[62] A. Konevskikh,[98] V. Kovalenko,[25] M. Kowalski,[49] S. Kox,[35] G. Koyithatta Meethaleveedu,[52] J. Kral,[38] I. Králik,[45] F. Kramer,[34] A. Kravčáková,[64] T. Krawutschke,[28] M. Krelina,[2] M. Kretz,[22] M. Krivda,[48,45] F. Krizek,[38] M. Krus,[2] E. Kryshen,[56] M. Krzewicki,[27] Y. Kucheriaev,[16] T. Kugathasan,[6] C. Kuhn,[53] P. G. Kuijer,[66] I. Kulakov,[34] J. Kumar,[52] P. Kurashvili,[95] A. Kurepin,[98] A. B. Kurepin,[98] A. Kuryakin,[70] S. Kushpil,[3] V. Kushpil,[3] H. Kvaerno,[97] M. J. Kweon,[28] Y. Kwon,[79] P. Ladrón de Guevara,[88] I. Lakomov,[90] R. Langoy,[24] S. L. La Pointe,[59] C. Lara,[61] A. Lardeux,[33] P. La Rocca,[47] R. Lea,[74] M. Lechman,[6] K. S. Lee,[42] G. R. Lee,[48] S. C. Lee,[42] I. Legrand,[6] J. Lehnert,[34] R. C. Lemmon,[116] M. Lenhardt,[27] V. Lenti,[94] H. León,[20] I. León Monzón,[103] H. León Vargas,[34] P. Lévai,[9] S. Li,[72] J. Lien,[24] R. Lietava,[48] S. Lindal,[97] V. Lindenstruth,[22] C. Lippmann,[27,6] M. A. Lisa,[30] H. M. Ljunggren,[83] D. F. Lodato,[59] P. I. Loenne,[24] V. R. Loggins,[65] V. Loginov,[62] D. Lohner,[28] C. Loizides,[67] K. K. Loo,[38] X. Lopez,[41] E. López Torres,[78] G. Løvhøiden,[97] X.-G. Lu,[28] P. Luettig,[34] M. Lunardon,[71] J. Luo,[72] G. Luparello,[59] C. Luzzi,[6] R. Ma,[4] K. Ma,[72] D. M. Madagodahettige-Don,[54] A. Maevskaya,[98] M. Mager,[110,6] D. P. Mahapatra,[46] A. Maire,[28] M. Malaev,[56] I. Maldonado Cervantes,[88] L. Malinina,[50,117] D. Mal'Kevich,[15] P. Malzacher,[27] A. Mamonov,[70] L. Manceau,[7] L. Mangotra,[43] V. Manko,[16] F. Manso,[41] N. Manukyan,[106] V. Manzari,[94] Y. Mao,[72] M. Marchisone,[41,55] J. Mareš,[118] G. V. Margagliotti,[74,100] A. Margotti,[17] A. Marín,[27] C. Markert,[115] M. Marquard,[34] I. Martashvili,[119] N. A. Martin,[27] P. Martinengo,[6] M. I. Martínez,[87] A. Martínez Davalos,[20]

G. Martínez García,[33] Y. Martynov,[19] A. Mas,[33] S. Masciocchi,[27] M. Masera,[55] A. Masoni,[85] L. Massacrier,[33] A. Mastroserio,[23] A. Matyja,[49] C. Mayer,[49] J. Mazer,[119] M. A. Mazzoni,[96] F. Meddi,[120] A. Menchaca-Rocha,[20] J. Mercado Pérez,[28] M. Meres,[69] Y. Miake,[57] K. Mikhaylov,[50,45,15] L. Milano,[55] J. Milosevic,[97,121] A. Mischke,[59] A. N. Mishra,[104,122] D. Miśkowiec,[27] C. Mitu,[89] S. Mizuno,[57] J. Mlynarz,[65] B. Mohanty,[11,123] L. Molnar,[9,53] L. Montaño Zetina,[75] M. Monteno,[7] E. Montes,[60] T. Moon,[79] M. Morando,[71] D. A. Moreira De Godoy,[76] S. Moretto,[71] A. Morreale,[38] A. Morsch,[6] V. Muccifora,[58] E. Mudnic,[105] S. Muhuri,[11] M. Mukherjee,[11] H. Müller,[6] M. G. Munhoz,[76] S. Murray,[39] L. Musa,[6] J. Musinsky,[45] B. K. Nandi,[52] R. Nania,[17] E. Nappi,[94] C. Nattrass,[119] T. K. Nayak,[11] S. Nazarenko,[70] A. Nedosekin,[15] M. Nicassio,[23,27] M. Niculescu,[89,6] B. S. Nielsen,[51] T. Niida,[57] S. Nikolaev,[16] V. Nikolic,[31] S. Nikulin,[16] V. Nikulin,[56] B. S. Nilsen,[81] M. S. Nilsson,[97] F. Noferini,[17,18] P. Nomokonov,[50] G. Nooren,[59] A. Nyanin,[16] A. Nyatha,[52] C. Nygaard,[51] J. Nystrand,[24] A. Ochirov,[25] H. Oeschler,[110,6,28] S. K. Oh,[42] S. Oh,[4] J. Oleniacz,[102] A. C. Oliveira Da Silva,[76] C. Oppedisano,[7] A. Ortiz Velasquez,[83,88] A. Oskarsson,[83] P. Ostrowski,[102] J. Otwinowski,[27] K. Oyama,[28] K. Ozawa,[107] Y. Pachmayer,[28] M. Pachr,[2] F. Padilla,[55] P. Pagano,[93] G. Paić,[88] F. Painke,[22] C. Pajares,[36] S. K. Pal,[11] A. Palaha,[48] A. Palmeri,[40] V. Papikyan,[106] G. S. Pappalardo,[40] W. J. Park,[27] A. Passfeld,[29] B. Pastirčák,[45] D. I. Patalakha,[63] V. Paticchio,[94] B. Paul,[80] A. Pavlinov,[65] T. Pawlak,[102] T. Peitzmann,[59] H. Pereira Da Costa,[44] E. Pereira De Oliveira Filho,[76] D. Peresunko,[16] C. E. Pérez Lara,[66] D. Perrino,[23] W. Peryt,[102] A. Pesci,[17] V. Peskov,[6] Y. Pestov,[124] V. Petráček,[2] M. Petran,[2] M. Petris,[26] P. Petrov,[48] M. Petrovici,[26] C. Petta,[47] S. Piano,[100] M. Pikna,[69] P. Pillot,[33] O. Pinazza,[6] L. Pinsky,[54] N. Pitz,[34] D. B. Piyarathna,[54] M. Planinic,[31] M. Płoskoń,[67] J. Pluta,[102] T. Pocheptsov,[50] S. Pochybova,[9] P. L. M. Podesta-Lerma,[103] M. G. Poghosyan,[6] K. Polák,[118] B. Polichtchouk,[63] N. Poljak,[59,31] A. Pop,[26] S. Porteboeuf-Houssais,[41] V. Pospíšil,[2] B. Potukuchi,[43] S. K. Prasad,[65] R. Preghenella,[17,18] F. Prino,[7] C. A. Pruneau,[65] I. Pshenichnov,[98] G. Puddu,[77] V. Punin,[70] M. Putiš,[64] J. Putschke,[65] H. Qvigstad,[97] A. Rachevski,[100] A. Rademakers,[6] T. S. Räihä,[38] J. Rak,[38] A. Rakotozafindrabe,[44] L. Ramello,[86] A. Ramírez Reyes,[75] S. Raniwala,[104] R. Raniwala,[104] S. S. Räsänen,[38] B. T. Rascanu,[34] D. Rathee,[5] K. F. Read,[119] J. S. Real,[35] K. Redlich,[95,125] R. J. Reed,[4] A. Rehman,[24] P. Reichelt,[34] M. Reicher,[59] R. Renfordt,[34] A. R. Reolon,[58] A. Reshetin,[98] F. Rettig,[22] J.-P. Revol,[6] K. Reygers,[28] L. Riccati,[7] R. A. Ricci,[126] T. Richert,[83] M. Richter,[97] P. Riedler,[6] W. Riegler,[6] F. Riggi,[47,40] M. Rodríguez Cahuantzi,[87] A. Rodriguez Manso,[66] K. Røed,[24,97] E. Rogochaya,[50] D. Rohr,[22] D. Röhrich,[24] R. Romita,[27,116] F. Ronchetti,[58] P. Rosnet,[41] S. Rossegger,[6] A. Rossi,[6,71] C. Roy,[53] P. Roy,[80] A. J. Rubio Montero,[60] R. Rui,[74] R. Russo,[55] E. Ryabinkin,[16] A. Rybicki,[49] S. Sadovsky,[63] K. Šafařík,[6] R. Sahoo,[122] P. K. Sahu,[46] J. Saini,[11] H. Sakaguchi,[127] S. Sakai,[67] D. Sakata,[57] C. A. Salgado,[36] J. Salzwedel,[30] S. Sambyal,[43] V. Samsonov,[56] X. Sanchez Castro,[53] L. Šándor,[45] A. Sandoval,[20] M. Sano,[57] G. Santagati,[47] R. Santoro,[6,18] J. Sarkamo,[38] E. Scapparone,[17] F. Scarlassara,[71] R. P. Scharenberg,[68] C. Schiaua,[26] R. Schicker,[28] H. R. Schmidt,[109] C. Schmidt,[27] S. Schuchmann,[34] J. Schukraft,[6] T. Schuster,[4] Y. Schutz,[6,33] K. Schwarz,[27] K. Schweda,[27] G. Scioli,[10] E. Scomparin,[7] R. Scott,[119] P. A. Scott,[48] G. Segato,[71] I. Selyuzhenkov,[27] S. Senyukov,[53] J. Seo,[84] S. Serci,[77] E. Serradilla,[60,20] A. Sevcenco,[89] A. Shabetai,[33] G. Shabratova,[50] R. Shahoyan,[6] S. Sharma,[43] N. Sharma,[5,119] S. Rohni,[43] K. Shigaki,[127] K. Shtejer,[78] Y. Sibiriak,[16] E. Sicking,[29] S. Siddhanta,[85] T. Siemiarczuk,[95] D. Silvermyr,[37] C. Silvestre,[35] G. Simatovic,[88,31] G. Simonetti,[6] R. Singaraju,[11] R. Singh,[43] S. Singha,[11,123] V. Singhal,[11] T. Sinha,[80] B. C. Sinha,[11] B. Sitar,[69] M. Sitta,[86] T. B. Skaali,[97] K. Skjerdal,[24] R. Smakal,[2] N. Smirnov,[4] R. J. M. Snellings,[59] C. Søgaard,[83] R. Soltz,[1] H. Son,[108] J. Song,[84] M. Song,[79] C. Soos,[6] F. Soramel,[71] I. Sputowska,[49] M. Spyropoulou-Stassinaki,[99] B. K. Srivastava,[68] J. Stachel,[28] I. Stan,[89] G. Stefanek,[95] M. Steinpreis,[30] E. Stenlund,[83] G. Steyn,[39] J. H. Stiller,[28] D. Stocco,[33] M. Stolpovskiy,[63] P. Strmen,[69] A. A. P. Suaide,[76] M. A. Subieta Vásquez,[55] T. Sugitate,[127] C. Suire,[90] R. Sultanov,[15] M. Šumbera,[3] T. Susa,[31] T. J. M. Symons,[67] A. Szanto de Toledo,[76] I. Szarka,[69] A. Szczepankiewicz,[49,6] M. Szymański,[102] J. Takahashi,[92] M. A. Tangaro,[23] J. D. Tapia Takaki,[90] A. Tarantola Peloni,[34] A. Tarazona Martinez,[6] A. Tauro,[6] G. Tejeda Muñoz,[87] A. Telesca,[6] A. Ter Minasyan,[16] C. Terrevoli,[23] J. Thäder,[27] D. Thomas,[59] R. Tieulent,[82] A. R. Timmins,[54] D. Tlusty,[2] A. Toia,[22,71,32] H. Torii,[107] L. Toscano,[7] V. Trubnikov,[19] D. Truesdale,[30] W. H. Trzaska,[38] T. Tsuji,[107] A. Tumkin,[70] R. Turrisi,[32] T. S. Tveter,[97] J. Ulery,[34] K. Ullaland,[24] J. Ulrich,[128,61] A. Uras,[82] G. M. Urciuoli,[96] G. L. Usai,[77] M. Vajzer,[2,3] M. Vala,[50,45] L. Valencia Palomo,[90] P. Vande Vyvre,[6] M. van Leeuwen,[59] L. Vannucci,[126] A. Vargas,[87] R. Varma,[52] M. Vasileiou,[99] A. Vasiliev,[16] V. Vechernin,[25] M. Veldhoen,[59] M. Venaruzzo,[74] E. Vercellin,[55] S. Vergara,[87] R. Vernet,[129] M. Verweij,[59] L. Vickovic,[105] G. Viesti,[71] J. Viinikainen,[38] Z. Vilakazi,[39] O. Villalobos Baillie,[48] L. Vinogradov,[25] Y. Vinogradov,[70] A. Vinogradov,[16] T. Virgili,[93] Y. P. Viyogi,[11] A. Vodopyanov,[50] M. A. Völkl,[28] S. Voloshin,[65] K. Voloshin,[15] G. Volpe,[6] B. von Haller,[6] I. Vorobyev,[25] D. Vranic,[27] J. Vrláková,[64] B. Vulpescu,[41] A. Vyushin,[70] V. Wagner,[2] B. Wagner,[24] R. Wan,[72] Y. Wang,[72] M. Wang,[72] D. Wang,[72] Y. Wang,[28] K. Watanabe,[57] M. Weber,[54] J. P. Wessels,[6,29] U. Westerhoff,[29] J. Wiechula,[109] J. Wikne,[97] M. Wilde,[29] A. Wilk,[29] G. Wilk,[95] M. C. S. Williams,[17] B. Windelband,[28] L. Xaplanteris Karampatsos,[115] C. G. Yaldo,[65] Y. Yamaguchi,[107] H. Yang,[44,59] S. Yang,[24] S. Yasnopolskiy,[16] J. Yi,[84] Z. Yin,[72] I.-K. Yoo,[84] J. Yoon,[79] W. Yu,[34] X. Yuan,[72] I. Yushmanov,[16] V. Zaccolo,[51] C. Zach,[2] C. Zampolli,[17] S. Zaporozhets,[50] A. Zarochentsev,[25] P. Závada,[118] N. Zaviyalov,[70] H. Zbroszczyk,[102] P. Zelnicek,[61] I. S. Zgura,[89] M. Zhalov,[56] X. Zhang,[67,41,72] H. Zhang,[72] Y. Zhou,[59] F. Zhou,[72] D. Zhou,[72] J. Zhu,[72] J. Zhu,[72] X. Zhu,[72] H. Zhu,[72] A. Zichichi,[10,18] A. Zimmermann,[28] G. Zinovjev,[19] Y. Zoccarato,[82] M. Zynovyev,[19] and M. Zyzak[34]

(ALICE Collaboration)

[1]*Lawrence Livermore National Laboratory, Livermore, California, USA*
[2]*Faculty of Nuclear Sciences and Physical Engineering, Czech Technical University in Prague, Prague, Czech Republic*

[3]*Nuclear Physics Institute, Academy of Sciences of the Czech Republic, Řež u Prahy, Czech Republic*
[4]*Yale University, New Haven, Connecticut, USA*
[5]*Physics Department, Panjab University, Chandigarh, India*
[6]*European Organization for Nuclear Research (CERN), Geneva, Switzerland*
[7]*Sezione INFN, Turin, Italy*
[8]*Politecnico di Torino, Turin, Italy*
[9]*Wigner Research Centre for Physics, Hungarian Academy of Sciences, Budapest, Hungary*
[10]*Dipartimento di Fisica e Astronomia dell'Università and Sezione INFN, Bologna, Italy*
[11]*Variable Energy Cyclotron Centre, Kolkata, India*
[12]*Department of Physics Aligarh Muslim University, Aligarh, India*
[13]*Korea Institute of Science and Technology Information, Daejeon, South Korea*
[14]*COMSATS Institute of Information Technology (CIIT), Islamabad, Pakistan*
[15]*Institute for Theoretical and Experimental Physics, Moscow, Russia*
[16]*Russian Research Centre Kurchatov Institute, Moscow, Russia*
[17]*Sezione INFN, Bologna, Italy*
[18]*Centro Fermi, Museo Storico della Fisica e Centro Studi e Ricerche "Enrico Fermi," Rome, Italy*
[19]*Bogolyubov Institute for Theoretical Physics, Kiev, Ukraine*
[20]*Instituto de Física, Universidad Nacional Autónoma de México, Mexico City, Mexico*
[21]*Faculty of Engineering, Bergen University College, Bergen, Norway*
[22]*Frankfurt Institute for Advanced Studies, Johann Wolfgang Goethe–Universität Frankfurt, Frankfurt, Germany*
[23]*Dipartimento Interateneo di Fisica "M. Merlin" and Sezione INFN, Bari, Italy*
[24]*Department of Physics and Technology, University of Bergen, Bergen, Norway*
[25]*V. Fock Institute for Physics, St. Petersburg State University, St. Petersburg, Russia*
[26]*National Institute for Physics and Nuclear Engineering, Bucharest, Romania*
[27]*Research Division and ExtreMe Matter Institute EMMI, GSI Helmholtzzentrum für Schwerionenforschung, Darmstadt, Germany*
[28]*Physikalisches Institut, Ruprecht-Karls-Universität Heidelberg, Heidelberg, Germany*
[29]*Institut für Kernphysik, Westfälische Wilhelms-Universität Münster, Münster, Germany*
[30]*Department of Physics, Ohio State University, Columbus, Ohio, USA*
[31]*Rudjer Bošković Institute, Zagreb, Croatia*
[32]*Sezione INFN, Padova, Italy*
[33]*SUBATECH, Ecole des Mines de Nantes, Université de Nantes, CNRS-IN2P3, Nantes, France*
[34]*Institut für Kernphysik, Johann Wolfgang Goethe-Universität Frankfurt, Frankfurt, Germany*
[35]*Laboratoire de Physique Subatomique et de Cosmologie (LPSC), Université Joseph Fourier, CNRS-IN2P3,*
Institut Polytechnique de Grenoble, Grenoble, France
[36]*Departamento de Física de Partículas and IGFAE, Universidad de Santiago de Compostela, Santiago de Compostela, Spain*
[37]*Oak Ridge National Laboratory, Oak Ridge, Tennessee, USA*
[38]*Helsinki Institute of Physics (HIP) and University of Jyväskylä, Jyväskylä, Finland*
[39]*Physics Department, University of Cape Town and iThemba LABS, National Research Foundation, Somerset West, South Africa*
[40]*Sezione INFN, Catania, Italy*
[41]*Laboratoire de Physique Corpusculaire (LPC), Clermont Université, Université Blaise Pascal, CNRS–IN2P3, Clermont-Ferrand, France*
[42]*Gangneung-Wonju National University, Gangneung, South Korea*
[43]*Physics Department, University of Jammu, Jammu, India*
[44]*Commissariat à l'Energie Atomique, IRFU, Saclay, France*
[45]*Institute of Experimental Physics, Slovak Academy of Sciences, Košice, Slovakia*
[46]*Institute of Physics, Bhubaneswar, India*
[47]*Dipartimento di Fisica e Astronomia dell'Università Sezione INFN, Catania, Italy*
[48]*School of Physics and Astronomy, University of Birmingham, Birmingham, United Kingdom*
[49]*The Henryk Niewodniczanski Institute of Nuclear Physics, Polish Academy of Sciences, Cracow, Poland*
[50]*Joint Institute for Nuclear Research (JINR), Dubna, Russia*
[51]*Niels Bohr Institute, University of Copenhagen, Copenhagen, Denmark*
[52]*Indian Institute of Technology Bombay (IIT), Mumbai, India*
[53]*Institut Pluridisciplinaire Hubert Curien (IPHC), Université de Strasbourg, CNRS-IN2P3, Strasbourg, France*
[54]*University of Houston, Houston, Texas, USA*
[55]*Dipartimento di Fisica dell'Università and Sezione INFN, Turin, Italy*
[56]*Petersburg Nuclear Physics Institute, Gatchina, Russia*
[57]*University of Tsukuba, Tsukuba, Japan*
[58]*Laboratori Nazionali di Frascati, INFN, Frascati, Italy*
[59]*Nikhef, National Institute for Subatomic Physics and Institute for Subatomic Physics of Utrecht University, Utrecht, Netherlands*

^{60}*Centro de Investigaciones Energéticas Medioambientales y Tecnológicas (CIEMAT), Madrid, Spain*

^{61}*Institut für Informatik, Johann Wolfgang Goethe-Universität Frankfurt, Frankfurt, Germany*

^{62}*Moscow Engineering Physics Institute, Moscow, Russia*

^{63}*Institute for High Energy Physics, Protvino, Russia*

^{64}*Faculty of Science, P. J. Šafárik University, Košice, Slovakia*

^{65}*Wayne State University, Detroit, Michigan, USA*

^{66}*Nikhef, National Institute for Subatomic Physics, Amsterdam, Netherlands*

^{67}*Lawrence Berkeley National Laboratory, Berkeley, California, USA*

^{68}*Purdue University, West Lafayette, Indiana, USA*

^{69}*Faculty of Mathematics, Physics and Informatics, Comenius University, Bratislava, Slovakia*

^{70}*Russian Federal Nuclear Center (VNIIEF), Sarov, Russia*

^{71}*Dipartimento di Fisica e Astronomia dell'Università and Sezione INFN, Padova, Italy*

^{72}*Central China Normal University, Wuhan, China*

^{73}*Sección Física, Departamento de Ciencias, Pontificia Universidad Católica del Perú, Lima, Peru*

^{74}*Dipartimento di Fisica dell'Università and Sezione INFN, Trieste, Italy*

^{75}*Centro de Investigación y de Estudios Avanzados (CINVESTAV), Mexico City and Mérida, Mexico*

^{76}*Universidade de São Paulo (USP), São Paulo, Brazil*

^{77}*Dipartimento di Fisica dell'Università and Sezione INFN, Cagliari, Italy*

^{78}*Centro de Aplicaciones Tecnológicas y Desarrollo Nuclear (CEADEN), Havana, Cuba*

^{79}*Yonsei University, Seoul, South Korea*

^{80}*Saha Institute of Nuclear Physics, Kolkata, India*

^{81}*Physics Department, Creighton University, Omaha, Nebraska, USA*

^{82}*Université de Lyon, Université Lyon 1, CNRS/IN2P3, IPN-Lyon, Villeurbanne, France*

^{83}*Division of Experimental High Energy Physics, University of Lund, Lund, Sweden*

^{84}*Pusan National University, Pusan, South Korea*

^{85}*Sezione INFN, Cagliari, Italy*

^{86}*Dipartimento di Scienze e Innovazione Tecnologica dell'Università del Piemonte Orientale and Gruppo Collegato INFN, Alessandria, Italy*

^{87}*Benemérita Universidad Autónoma de Puebla, Puebla, Mexico*

^{88}*Instituto de Ciencias Nucleares, Universidad Nacional Autónoma de México, Mexico City, Mexico*

^{89}*Institute of Space Sciences (ISS), Bucharest, Romania*

^{90}*Institut de Physique Nucléaire d'Orsay (IPNO), Université Paris-Sud, CNRS-IN2P3, Orsay, France*

^{91}*Bose Institute, Department of Physics and Centre for Astroparticle Physics and Space Science (CAPSS), Kolkata, India*

^{92}*Universidade Estadual de Campinas (UNICAMP), Campinas, Brazil*

^{93}*Dipartimento di Fisica "E. R. Caianiello" dell'Università and Gruppo Collegato INFN, Salerno, Italy*

^{94}*Sezione INFN, Bari, Italy*

^{95}*National Centre for Nuclear Studies, Warsaw, Poland*

^{96}*Sezione INFN, Rome, Italy*

^{97}*Department of Physics, University of Oslo, Oslo, Norway*

^{98}*Institute for Nuclear Research, Academy of Sciences, Moscow, Russia*

^{99}*Physics Department, University of Athens, Athens, Greece*

^{100}*Sezione INFN, Trieste, Italy*

^{101}*Chicago State University, Chicago, USA*

^{102}*Warsaw University of Technology, Warsaw, Poland*

^{103}*Universidad Autónoma de Sinaloa, Culiacán, Mexico*

^{104}*Physics Department, University of Rajasthan, Jaipur, India*

^{105}*Technical University of Split FESB, Split, Croatia*

^{106}*A. I. Alikhanyan National Science Laboratory (Yerevan Physics Institute) Foundation, Yerevan, Armenia*

^{107}*University of Tokyo, Tokyo, Japan*

^{108}*Department of Physics, Sejong University, Seoul, South Korea*

^{109}*Eberhard Karls Universität Tübingen, Tübingen, Germany*

^{110}*Institut für Kernphysik, Technische Universität Darmstadt, Darmstadt, Germany*

^{111}*Yildiz Technical University, Istanbul, Turkey*

^{112}*KTO Karatay University, Konya, Turkey*

^{113}*Zentrum für Technologietransfer und Telekommunikation (ZTT), Fachhochschule Worms, Worms, Germany*

^{114}*California Polytechnic State University, San Luis Obispo, California, USA*

^{115}*The University of Texas at Austin, Physics Department, Austin, Texas, USA*

^{116}*Nuclear Physics Group, STFC Daresbury Laboratory, Daresbury, United Kingdom*

^{117}*M. V. Lomonosov Moscow State University, D. V. Skobeltsyn Institute of Nuclear Physics, Moscow, Russia*

[118]*Institute of Physics, Academy of Sciences of the Czech Republic, Prague, Czech Republic*
[119]*University of Tennessee, Knoxville, Tennessee, USA*
[120]*Dipartimento di Fisica dell'Università "La Sapienza" and Sezione INFN, Rome, Italy*
[121]*University of Belgrade, Faculty of Physics and "Vinča" Institute of Nuclear Sciences, Belgrade, Serbia*
[122]*Indian Institute of Technology Indore, Indore, India (IITI)*
[123]*National Institute of Science Education and Research, Bhubaneswar, India*
[124]*Budker Institute for Nuclear Physics, Novosibirsk, Russia*
[125]*Institut of Theoretical Physics, University of Wroclaw, Wroclaw, Poland*
[126]*Laboratori Nazionali di Legnaro, INFN, Legnaro, Italy*
[127]*Hiroshima University, Hiroshima, Japan*
[128]*Kirchhoff-Institut für Physik, Ruprecht-Karls-Universität Heidelberg, Heidelberg, Germany*
[129]*Centre de Calcul de l'IN2P3, Villeurbanne, France*